UNIVERSITY OF CALIFORNIA SAN DIEGO

Engineering and utilizing nonlinear and electro-optic properties of silicon and silicon-nitride waveguides

A dissertation submitted in partial satisfaction of the

requirements for the degree Doctor of Philosophy

in

Electrical Engineering (Photonics)

by

Rajat Sharma

Committee in charge:

      Professor Yeshaiahu Fainman, Chair
      Professor Prabhakar Bandaru
      Professor Shadi Dayeh
      Professor Andrew Kummel
      Professor Yu-Hwa Lo

2019

The Dissertation of Rajat Sharma is approved, and is acceptable in quality and form for publication on microfilm and electronically:

_____

_____

_____

_____

_____

Chair

University of California San Diego

2019

TABLE OF CONTENTS

LIST OF FIGURES

<center>LIST OF TABLES</center>

ACKNOWLEDGEMENTS

First and foremost, I'd like to acknowledge that this would most certainly not be possible without the guidance of my committee members, help from colleagues, and unwavering support from my friends and family.

I would like to express my deepest gratitude to my advisor, Prof. Fainman, for hiring me on as a graduate student and then allowing me to pursue my research ideas freely. Working in Shaya's group truly allows one to experiences all facets of academia and appreciate the process from the bottom to the very top. I would also like to thank Prof. Dayeh, Prof. Lo, Prof. Kummel and Prof. Bandaru for agreeing to be on my doctoral committee and for giving me valuable advice during my exams and during the course of my research.

I especially want to thank my former colleague, Dr. Matthew Puckett, without whom my research would have never taken off and who will always remain a most cherished friend. I'd also like to thank my colleagues, Hani Nejadriahi, Alex Friedman, Hung-Hsi Lin, Felipe Vallini and Joseph Smalley, who were always helpful in my research and my life and formed the core of my friend circle in San Diego. San Diego felt like home because of these guys.

Finally, I would like to thank my parents and my elder sister, Rachita Sharma, for their constant support and wishes. Nothing in my life, from graduating high school to writing this dissertation, would have come to be without these guys. They stood by me during the toughest times and never lost faith in me. Thank you and I love you guys!

Chapter 2, in part, contains materials from "Characterizing the effects of free carriers in fully etched, dielectric-clad silicon waveguides", published in Applied Physics Letters. This paper was co-authored by Matthew W. Puckett, Hung-Hsi Lin, Felipe Vallini and Yeshaiahu Fainman. The dissertation author was the first author of the manuscript.

Chapter 3, in part, contains materials from ""Effect of dielectric claddings on the electro-optic behavior of silicon waveguides", published in Optics Letters and co-authored by M.W. Puckett, H. Lin, A. Isichenko, F. Vallini, and Y. Fainman. The dissertation author was the first author of the manuscript.

Chapter 4, in part, contains materials from "Observation of second-harmonic generation in silicon nitride waveguides through bulk nonlinearities" published in Optics Express and co-authored by Matthew Puckett, Hung-Hsi Lin, Mu-Han Yang, Felipe Vallini and Yeshaiahu Fainman. The dissertation author was the first author the manuscript.

Chapter 5, in part, contains materials from "On the observation of dispersion in tunable second-order nonlinearities of silicon-rich nitride thin films." published in APL Photonics and co-authored by Hung-Hsi Lin, Alex Friedman, Benjamin M. Cromey, Felipe Vallini, M. W. Puckett, Khanh Kieu, and Yeshaiahu Fainman. The dissertation author was the first author the manuscript.

VITA

2012   Bachelor of Technology, Indian Institute of Technology Madras, India

2012   Master of Technology, Indian Institute of Technology Madras, India

2019   Doctor of Philosophy, University of California San Diego, USA

JOURNAL PUBLICATIONS

- **R. Sharma** Matthew W. Puckett, Hung-Hsi Lin, Felipe Vallini and Yeshaiahu Fainman. "Characterizing the effects of free carriers in fully etched, dielectric-clad silicon waveguides." Applied Physics Letters 106, 241104 (2015)

- **R. Sharma**, M.W. Puckett, H. Lin, A. Isichenko, F. Vallini, and Y. Fainman, "Effect of dielectric claddings on the electro-optic behavior of silicon waveguides." Optics Letters, Vol. 41, 6, March 2016

- M. W. Puckett*, **R. Sharma***, Hung-Hsi Lin, Mu-han Yang, Felipe Vallini, and Yeshaiahu Fainman. "Observation of second-harmonic generation in silicon nitride waveguides through bulk nonlinearities." *Optics express* 24, no. 15 (2016): 16923-16933. (***co first authors**)

- M. W. Puckett*, **R. Sharma***, Felipe Vallini, Shiva Shahin, Faraz Monifi, Peter N. Barrina, Soroush Mehravar, Khanh Kieu, and Yeshaiahu Fainman, "Silicon nanoridge array waveguides for nonlinear and sensing applications." Optics Express 23, no.22 (2015):28224-28233 (***co first authors**)

- **R. Sharma**, Hung-Hsi Lin, Alex Friedman, Benjamin M. Cromey, Felipe Vallini, M. W. Puckett, Khanh Kieu, and Yeshaiahu Fainman "On the observation of dispersion in tunable second-order nonlinearities of silicon-rich nitride thin films." Accepted, APL Photonics

- H. Lin, F. Vallini, M. Yang, **R. Sharma**, M. W. Puckett, S. Montoya, C. D. Wurm, E. E. Fullerton & Y. Fainman, "Electronic Metamaterials with Tunable Second-order Optical Nonlinearities." Scientific Reports 7, Article number: 9983 (2017)

- H. Lin, M. Yang, **R. Sharma**, M. W. Puckett, S. Montoya, C. D. Wurm, F. Vallini, E. E. Fullerton, and Y. Fainman, "Synthesis of second-order nonlinearities in dielectric-semiconductor-dielectric metamaterials." Applied Physics Letters 110, 113103 (2017)

ABSTRACT OF THE DISSERTATION

Engineering and utilizing nonlinear and electro-optic properties of silicon and silicon nitride waveguides

by

Rajat Sharma

Doctor of Philosophy in Electrical Engineering (Photonics)

University of California San Diego, 2019

Professor Yeshaiahu Fainman, Chair

Silicon photonics as a platform is on the cusp of commercialization on a large scale with the future of on-chip communication likely to be opto-electronic in nature. One of the most essential components of any such on-chip opto-electronic link is the modulator, which encodes an electrical signal onto an optical carrier. Despite decades of research and a multitude of results. presented by both academia and industry. there is still not one solution that satisfies all the requirements of high bandwidth, modulation efficiency, linearity, low power consumption and footprint simultaneously. Bulk of the research has gone into studying

the so-called free-carrier plasma dispersion effect, wherein a change in free-carrier, electron and hole, concentrations induces a change in complex refractive index of a material. This effect is utilized by means of either co-realizing a silicon-insulator-silicon (SIS) capacitor or a diode (p-n, p-i-n or other exotic junction schemes) with a silicon waveguide. Upon application of a voltage, a change in carrier concentration is induced which leads to a change in index. This is then used to achieve a change in phase of a propagating optical signal and then used ultimately, by means of devices such as Mach-Zehnder Interferometers or ring-resonators, to achieve intensity modulation.

In this thesis however, we propose an alternate solution to the problem. This is done by engineering effective nonlinearities in waveguides in the silicon photonics platform. As the two most popular materials used in the platform, we explore both silicon and silicon nitride as possible candidates and then propose and demonstrate methods to engineer and enhance nonlinearities in each.

In silicon, we explore the usage of dielectric/semiconductor interface fixed charges as means of altering silicon's electro-optic and nonlinear properties. We show for the first time that the dielectric fixed charges, by means of their magnitude and nature (positive or negative), can alter both passive and active properties of a silicon waveguide. This is then experimentally illustrated by analyzing the differences in the electro-optic response of dielectric (SiO$_2$, SiN$_x$ and Al$_2$O$_3$) clad silicon micro-ring resonators. It is conclusively demonstrated that a change in sign of the interfacial charge can reverse the slope of the observed electro-optic shift in the refractive index. These interfacial charges are then also shown to affect passive properties of waveguides, by means of changing the loss in the waveguide as well, and perhaps more importantly, by inducing a high electric-field within the waveguide even in the absence of an applied electric-field. This high electric-field, can then interact with crystalline silicon's relatively high third-order nonlinear susceptibility $\chi^{(3)}$, to give rise to an apparent/induced $\chi^{(2)}$. This is shown to be the major (dominating) cause behind the results presented in literature on second-harmonic generation in strained

silicon waveguides, wherein strain was hypothesized as a means of breaking silicon's centrosymmetry and inducing a non-zero $\chi^{(2)}$.

In silicon-nitride (SiN_x), our research was primarily focused on exploring the possibility of inducing a second-order nonlinearity in PECVD deposited thin-films. Within the purview of silicon photonics, silicon nitride has been shown to be a great material which has the simultaneous benefits of a large transparency window (large optical bandgap), ultra-low loss and CMOS computability. However, the use of the material has primarily only been for passive applications and or for wave-mixing based on its $\chi^{(3)}$, which is relatively low when compared to that of silicon.

In this thesis we present our results on the first demonstration of phase-matched second-harmonic generation in PECVD stoichiometric silicon nitride waveguides, conclusively shown to be due to bulk nonlinearities. Before this work, one result by Michal Lipson's group had shown resonant, phase-matched second-harmonic generation, attributing the phenomenon to interfacial nonlinearties and coefficient as low as 0.04pm/V. Our marked an improvement of upto two orders of magnitude in reported coefficient in silicon-nitride waveguides with measurements using a CW pump at 1550nm yielding a coefficient as high as 0.2pm/V and free-space measurements carried out 800nm pump yielding values as high as ~2pm/V. Simultenously, we were also the first to demonstrate the so-called electric-field induced second-harmonic (EFISH) effect in silicon-nitride waveguides, wherein an external voltage was used to "modulate" the SHG signal from silicon nitride waveguides.

Finally, we were also able to experimentally demonstrate a material-based approach towards enhancing PECVD silicon nitride's nonlinearities. This was done via increasing the films' silicon content resulting in so-called silicon-rich-nitride (SRN). The $\chi^{(2)}$ coefficients of such films, with indices ranging from 1.99 (stoichiometric) to 2.5 (silicon-rich), were found to increase with their silicon content, with the highest as-deposited coefficient measured being 8pm/V, using a pump at 800nm. The exhibited $\chi^{(2)}$ of these

films was further found to be dispersive with an enhancement of upto 6 times being achieved by changing the pump wavelength from 1550 to 1040nm.

CHAPTER 1
INTRODUCTION

Silicon is the primary candidate for the advancement of integrated photonics due to its prevalence within the electronics industry. One of the material's most notable shortcomings, however, is its centrosymmetry, which causes it to lack a second-order nonlinear susceptibility, disallowing electro-optic modulation based on the Pockels effect. To circumvent this complication, research efforts involving electro-optic modulation in silicon waveguides have instead exploited the free-carrier plasma dispersion effect, in which a change in the concentration of holes and electrons, generated by an electrical current, leads to deviations in both the real and imaginary parts of a semiconductor's index of refraction. Additionally, some work over the past decade has been devoted to exploring the strain-induced second-order nonlinear susceptibility in silicon. By deforming silicon's diamond lattice in an asymmetric way, it is possible to remove the material's centrosymmetry, thereby generating a second-order nonlinearity within the material. In recent works, values as high as 330 pm/V have been reported for the $\chi^{(2)}$ coefficient in strained silicon waveguides.
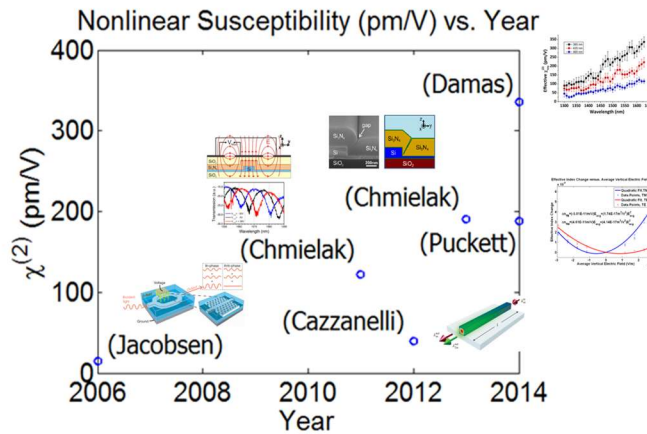
Figure. 1.1. Progress made in reported values of induced second-order nonlinear susceptibility ($\chi^{(2)}$ in pm/V) in strained silicon waveguides

Recently, however, it has been found that strained silicon's electro-optic effect is roughly quadratic in nature, rather than linear, as would be expected for the Pockels effect. Furthermore, many demonstrations of strained silicon's nonlinear properties have incorrectly assumed that the electric field, used to control silicon's index of refraction, penetrates strongly into the semiconductor waveguide itself [6-10], and this is known to have led to inaccurately reported nonlinear coefficients. Instead, the observed behavior in strained silicon waveguides is now thought to be due to the capacitively-induced free-carrier effect, which has already been used to demonstrate high-bandwidth modulation. Similarly, the wave-mixing observed in the literature for strained silicon waveguides has been attributed largely to electric field-induced second-harmonic generation.
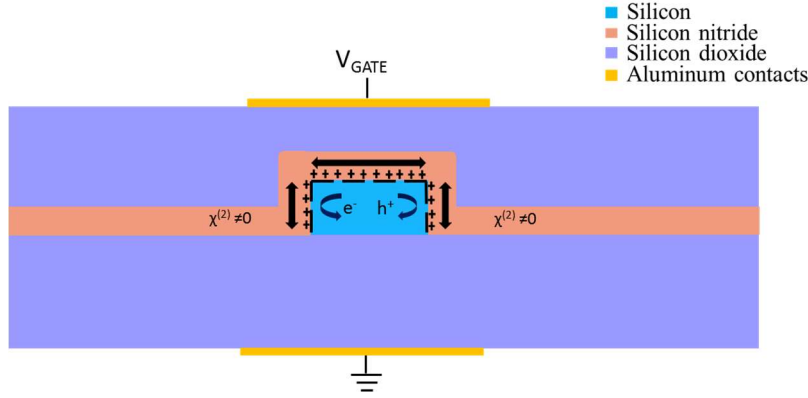
Figure. 1.2. Schematic representation of strained silicon waveguide clad with a stressor nitride layer. Shown are interfacial charges at the Si/SiN$_x$ interface and capacitive induction of free-carriers in the core of the waveguide upon application of a voltage using Aluminum contact pads

As such, there is an acute need for a highly nonlinear material that can be integrated on-chip to achieve efficient, high-speed, linear electro-optic modulation and nonlinear wave mixing in the silicon photonics platform.

Our approach was to investigate the possibility of achieving this goal without the need for any heterogenous integration. The two materials investigated were silicon and silicon nitride, both of which

have been widely employed to achieve several on-chip functionalities in recent years and are considered CMOS compatible. A summary of this work is as follows:

- Develop an understanding of the causative mechanisms contributing towards the "exhibited" second-order nonlinearity in strained silicon waveguides.
    - Capacitive plasma dispersion effect in dielectric clad silicon waveguides
    - Decoupling and quantitative estimation of the contribution of free-carrier effects towards exhibited electro-optic properties of strained silicon waveguides
    - Identify/quantify the causative agent behind demonstrations of second-harmonic generation in strained silicon waveguides
- Explore the possibility of engineering and enhancing nonlinear properties (second- and third-order nonlinear susceptibilities, $\chi^{(2)}$ and $\chi^{(3)}$) of silicon nitride
    - Free-space and in-waveguide demonstration of nonlinear wavemixing in PECVD deposited stoichiometric and silicon-rich nitride
    - Material engineering and electrical approaches towards enhancing as-deposited nonlinear properties of silicon nitride thin-films.
- Utilize this understanding of effective and engineered nonlinearities in silicon and silicon nitride towards the realization of an efficient, linear electro-optic modulator in silicon photonics.

Traditionally silicon and silicon nitride have never been seen as potential candidate towards achieving either linear electro-optic modulation or second-order wavemixing. Silicon nitride, to provide some background, has emerged as one such promising candidate with salient features such as a wide transparency window, ease of fabrication and compatibility with silicon photonics manufacturing. Conventionally,

silicon nitride has been viewed as a centrosymmetric dielectric, lacking any second-order nonlinear susceptibility, recent results in literature have shown that silicon nitride can exhibit an anomalous second-order nonlinear susceptibility, the origin of which remains unclear.

In this thesis, we undertake a systematic approach towards understanding, engineering and enhancing the effect electro-optic and nonlinear properties of silicon nitride and dielectric-clad silicon waveguides.

Chapter 2 describes the behavior and importance of understanding the interface of dilelectric claddings and silicon waveguides. These interfaces are shown to have a major impact on not just the active electro-optic but also the passive characteristics of silicon waveguides. This point is illustrated through measured CV characeristics of dielectric (SiO_2, SiN_x and Al_2O_3) thin films on silicon substrates to quantify the so-called the interfacial surface charge (Q_f). The effect of the magnitude and nature of this interfacial charge is then demonstrated through detailed SILVACO and LUMERICAL simuations showing a change in both real and imaginary part of refractive index as a function of voltage, induced due to the capacitively free-carried induced plasma dispersion effect. **This is conclusively shown to be the most dominant mechanism responsible for the demonstrated electro-optic and nonlinear properties of strained-silicon waveguides.**

Chapter 3 describes the experimental verification of our hypothesis by means of electro-optic characterization of bus-coupled ring-resonators. The waveguides forming the ring-resonators were fully-etched silicon ridge waveguides clad in each case with 50nm of SiO_2,

SiN_x and Al_2O_3. Voltages ranging from -30 to 30V were then applied to ring-resonators in each case, and the spectral shift observed was used to back calculated the change in real and imaginary part. The experimental results were found to be in close correspondence with the simulated results.

Chapter 4 describes our in-waveguide and free-space characterizations of second-order nonlinearities in stoichiometric silicon nitride thin-films. **We demonstrated for the first time, in-waveguide, phase-matched second-harmonic generation in silicon nitride waveguides. Along with passive second-harmonic generation, this was also the very first demonstration of electric-field induced second harmonic effect (EFISH) in silicon nitride waveguides.** EFISH was hence shown to be a viable means to achieve an enhancement in second-harmonic generation efficiency by means of artificially increasing the nonlinear coefficient. The nonlinearities were also simultaneously measured using an free-space Maker-fringes setup, using a pulsed fs source at 800nm. The measurement clearly demonstrated a disparity in values of the coefficient measured using pump wavelengths at 1550 and 800nm. This dispersion in the $\chi^{(2)}$ had never been reported on before.

Chapter 5 describes our results on enhancement of $\chi^{(2)}$ coefficient of silicon nitride films via two different approaches, namely:

- Increasing the silicon content in these films resulting in so-called silicon-rich-nitride (SRN) films with indices as high as 2.5, and a highest coefficient of 8pm/V in as-deposited films and measured at 800nm.

- The EFISH effect introduced in the last chapter, via which a SRN film with index of 2.5, sandwiched between two electrodes was experimentally demonstrated to exhibit an effective nonlinear coefficient of 22.7 pm/V, which is the highest reported to date in silicon nitride thin-films.

This approach of engineering nonlinear properties of silicon nitride based on enhancing as-deposited $\chi^{(2)}$ coefficient and further enhancement using the EFISH effect (and through the materials's $\chi^{(3)}$ coefficient) is shown to be extremely promising towards the realization of an efficient, capacitive electro-optic modulation using purely CMOS compatible materials.

Chapter 6 summarizes the research contributions of this dissertation and proposes possible future research directions.

Chapter 2

Dielectric claddings and their effect on electro-optic properties of silicon waveguides

2.1 Background

In the ongoing effort to realize low-loss, high-energy efficiency, and high-bandwidth active device components in nanoscale waveguides, one of the most direct ways to control the propagation of a guided mode is through the application of a capacitive bias electric field. In particular, materials such as lithium niobate or electro-optic polymers have been shown to exhibit large second-order nonlinear susceptibilities, making them desirable materials for the realization of on-chip nonlinear devices. More recently, strained silicon has emerged as another candidate for similar applications, despite its comparatively low nonlinear coefficients, due to its CMOS compatibility [1-7]. However, emerging research suggests that the analysis of semiconductor waveguides subjected to a DC electric field may be more complex than originally anticipated [8.,9]. In particular, band-bending and consequent redistribution of carriers at silicon-dielectric interfaces is anticipated to change both the real and the imaginary parts of silicon's refractive index. Additionally, large electric fields may be present in such waveguides, even in the absence of an applied bias, due to fixed interface charges in the dielectric films. Although these effects are gradually gaining attention within the framework of integrated photonics, more work still needs to be done to decouple free-carrier effects from other distinct properties of silicon waveguides.

In this chapter, we theoretically quantify the aforementioned changes in lightly doped p-type silicon waveguides, assuming they have been clad with either silicon dioxide, silicon nitride, or aluminum oxide. In addition to possessing distinct indices of refraction, each of the considered cladding materials is known to have different densities of (1) fixed charge and (2) interface trap states at interfaces with (100) silicon

[10]. Through our analysis, we find that these differences lead to large changes in the concentration of holes and electrons within the waveguide, even in the absence of a bias electric field. The different changes in carrier concentration are then found to have unique and noteworthy impacts on the modes supported by each of the waveguides under consideration. Furthermore, we show that the changes in carrier concentration in these waveguides in response to externally applied bias electric fields are dominant in determining the value of the field within the waveguide. This last point is particularly important to bear in mind in the characterization of active, capacitively driven silicon modulators.

2.2 MEASUREMENT OF DIELECTRIC FILM PROPERTIES

When a semiconductor comes into contact with a dielectric, the semiconductor's valence and conduction band energies may locally deviate from their natural values, leading to perturbations away from the material's bulk carrier concentrations [11]. To determine the extent to which this basic effect occurs, two non-idealities to consider are the concentration of fixed charges within the dielectric and the density of interface trap states. Whereas the former may shift the semiconductor's response to an externally applied bias voltage one way or the other, the latter may reduce the magnitude of this response altogether. In a silicon waveguide, any changes in the guiding material's carrier concentrations will produce a change in its optical properties, so it is vital to take these effects into consideration.

To determine the fixed charge present at a semiconductor-dielectric interface, the most common technique is to analyze a C-V measurement for a MOS structure consisting of the materials of interest. Because the fixed charge itself has a biasing effect on the carriers within the semiconductor, it tends to offset the response of the MOS structure to external voltages. By observing the experimental flat-band voltage of the device and comparing it to the theoretical value, the concentration of fixed charge in the dielectric may be calculated as [12]:

$$Q_f = C_{dielectric}(\Delta\varphi_{ms} - V_{FB}) \tag{2.1}$$

where $C_{dielectric}$ is the dielectric capacitance per unit area, $\Delta\varphi_{ms}$ is the difference in work function between the metal and the semiconductor (and therefore the flat-band voltage in the absence of any dielectric non-idealities), and V_{FB} is the measured flat-band voltage. It is important to note that the total fixed charge within the dielectric may change with the applied voltage due to bulk charge traps within the dielectric, potentially leading to hysteresis in the C-V measurement. But because we are only interested in order-of-magnitude analyses of the previously outlined effects of free carriers, and additionally because we are not considering the application of voltages large enough to induce appreciable hysteresis, we may neglect this complication.

In comparison to fixed charge, interface trap states are not necessarily charged, but rather may become positively or negatively charged in response to any field present at the semiconductor interface. Acceptor-type trap states may take an electron from the semiconductor and thus become negatively charged, and similarly donor-type trap states may give an electron to the semiconductor and become positively charged. The magnitude and sign of interface charge is therefore dependent upon the voltage applied across the MOS structure, as well as the type of interface state present. Because interface states have long response times, their effects will not affect high-frequency capacitance measurements. As a result, at the bias voltage corresponding to the minimum low-frequency capacitance the interface state density may be calculated as [13]:

$$D_{it} = \frac{C_{dielectric}}{q}\left(\frac{C_{LF}}{C_{dielectric} - C_{LF}} - \frac{C_{HF}}{C_{dielectric} - C_{HF}}\right) \tag{2.2}$$

where q is the electron charge, C_{LF} is the low-frequency capacitance per unit area of the total MOS structure, and C_{HF} is the corresponding high-frequency term.

To obtain these values for silicon dioxide and silicon nitride, we fabricated two MOS structures, one consisting of each material. Using an Oxford Plasma-Enhanced Chemical Vapor Depositor (PECVD), we deposited 150 nm of silicon dioxide and 180 nm of silicon nitride, respectively, on two silicon wafers doped with boron at a concentration of 1e15 cm^{-3}. PECVD was the chosen deposition technique both because of its prevalence in most waveguide fabrication processes and its CMOS compatibility. It should be noted that the target thickness was 150 nm for both dielectric layers, and that the variation exhibited by the silicon nitride layer resulted from fabrication imprecision. We then fabricated 200 nm-thick aluminum contacts on top of the dielectrics via photolithography and electron beam evaporation. Finally, we carried out a rapid thermal anneal (RTA) on both samples at a temperature of 300 °C for 15 minutes in a forming gas (N_2/H_2 : 90/10%) ambient to improve film quality. Once fabrication was complete, we carried out low- and high-frequency C-V measurements using an Agilent B1500A Semiconductor Device Analyzer [14]. The C-V curves, generated by scanning from a negative to positive voltage, are shown for the two materials in Fig. 1a and 1b. For the case of aluminum oxide, as well as the buried silicon dioxide, the values of interest were taken from the literature [10]. Specific properties of the interface traps such as the electron and hole recombination lifetimes were taken from the

literature as well [15,16]. The fixed charge and interface state densities for each of the materials under consideration are listed in Table 1.
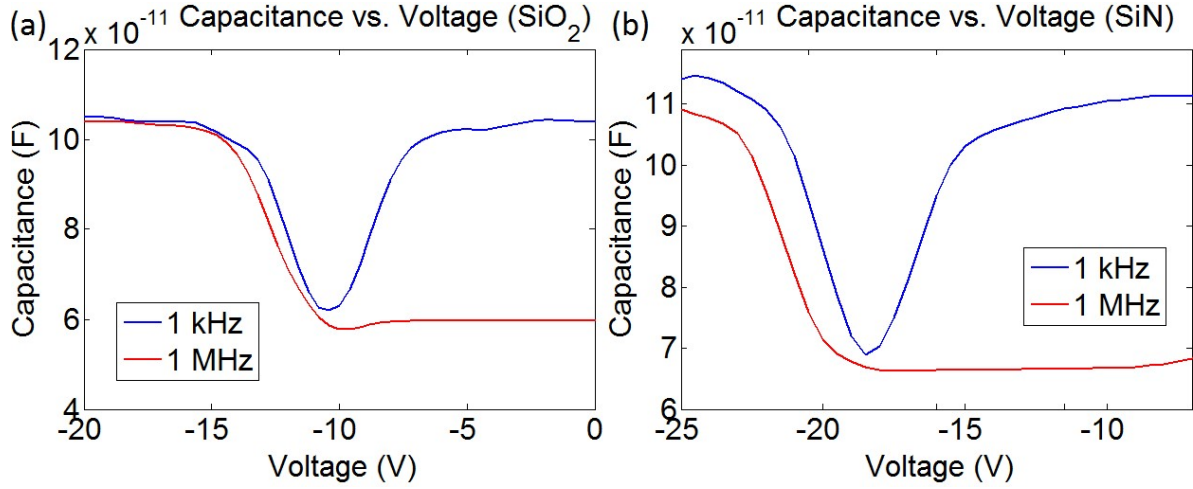
Figure. 2.1. Measured C-V characteristics showing the low- and high-frequency capacitance as a function of the bias voltage for (a) silicon dioxide and (b) silicon nitride films.

Table 2.1 Charge densities in dielectric films.

Material	Q_f (C/cm^{-2})	D_{it} (cm^{-2} eV^{-1})
PECVD SiO$_2$	1 x 10^{12}	2.5 x 10^{10}
PECVD SiN$_x$	3 x 10^{12}	2.1 x 10^{10}
ALD Al$_2$O$_3$	-2.2 x 10^{12}	1.1 x 10^{11}
Buried SiO$_2$	4 x 10^{10}	1.3 x 10^{10}

It is important to mention that in the fabrication and characterizaton of MOS structures, the quality of the interface is of paramount importance. If the surface cleaning is not perfect, a lossy dielectric layer will form between the semiconductor surface and the deposited film [17]. One of the more well-known results of this nonideality is a frequency dependent capacitance, specifically in the accumulation region, as is observed in the reported C-V measurements of the silicon nitride film. This however impacts neither the determination of fixed nor interface trap charges [10].

11

2.3 ELECTRO OPTIC MODELLING

2.3.1 SILVACO MODELLING OF CARRIER PROFILES

Based on the obtained experimental and theoretical values, we created two-dimensional models using the semiconductor physics tool Silvaco to determine the concentration of holes and electrons across a 250 nm-tall, 500 nm-wide silicon waveguide clad with each of the aforementioned dielectrics [18]. A cladding thickness of 1 μm was chosen in order to eliminate metallic optical absorption, and a vertical electrode configuration was assumed because it is a common technique in the characterization of strained silicon and other electo-optic materials [1,5]. By changing the bias voltage applied vertically across the simulation space, we were further able to observe how free carriers affected the electric fields induced within the waveguides. Cross-sectional plots of the electron (minority carrier) concentrations are shown in Fig. 2a-2f for both the negatively and positively biased cases, and for each of the materials under consideration. Also, Fig. 2g shows the geometry assumed in the model. For the waveguides with either silicon dioxide or silicon nitride cladding, the positive fixed interface charges push the silicon into depletion, whereas the negative fixed charge inherent to the aluminum oxide leads to accumulation. Moreover, although the voltages applied across the waveguide lead to changes in carrier concentration, the sign and magnitude of this change is largely governed by the fixed charge density, as will be subsequently discussed in greater detail.
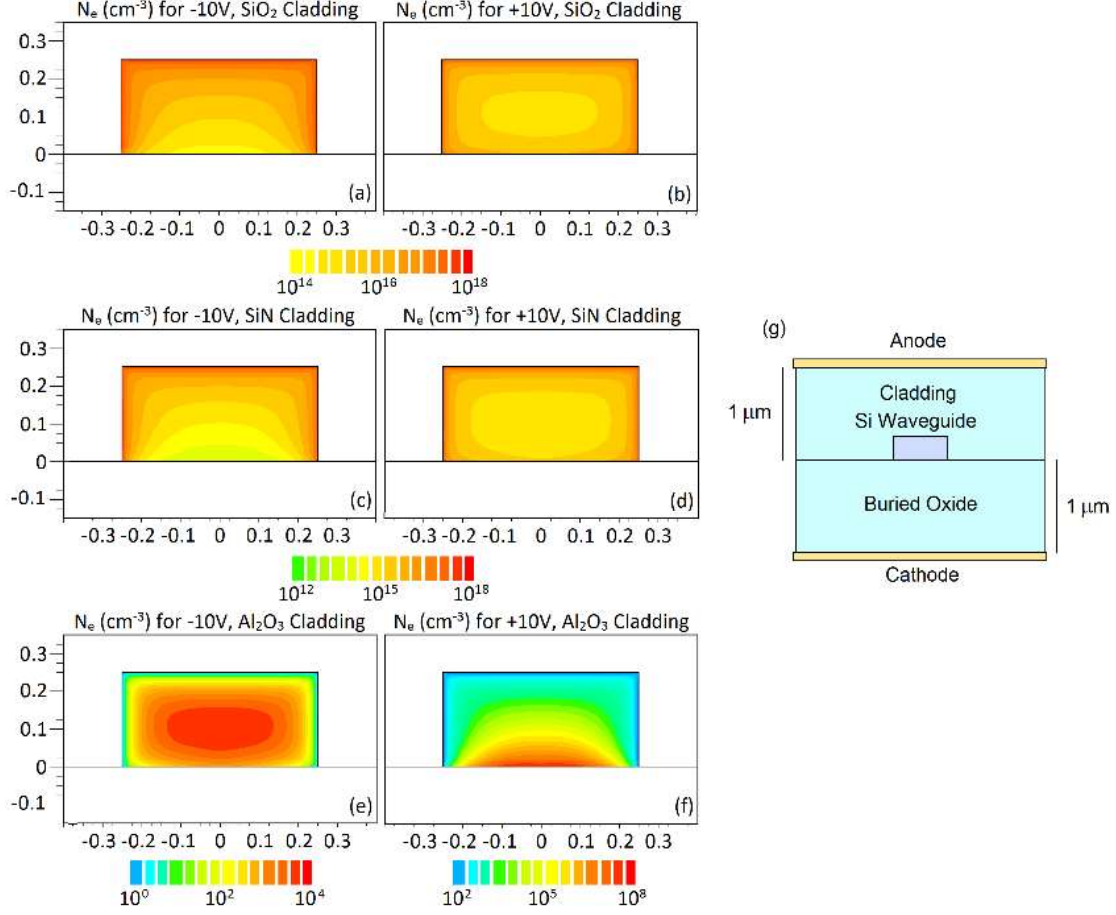
Figure. 2.2. Electron concentrations across silicon waveguides, assuming vertical bias voltages of either -10 V (left column) or +10 V (right column), when the cladding material is (a,b) silicon dioxide, (c,d) silicon nitride, or (e,f) aluminum oxide. Spatial dimensions are given in units of microns. (g) Illustration of the geometry used in Silvaco.

To further consider the interaction between silicon's free carriers and the electric field in the waveguides, we additionally observed the electrostatic behavior of the waveguide clad with silicon nitride. Our results, shown in Fig. 3, highlight the shielding effect provided by the carriers. When applying a bias of 10 V, the average and the peak value of the electric field (plotted along a y-slice at the center of the waveguide in Fig. 3) show minimal changes from their no-bias value, despite the large field values present just beyond the waveguide's boundaries. This illustrates how well free carriers may reduce the interaction of silicon with capacitively applied bias fields.
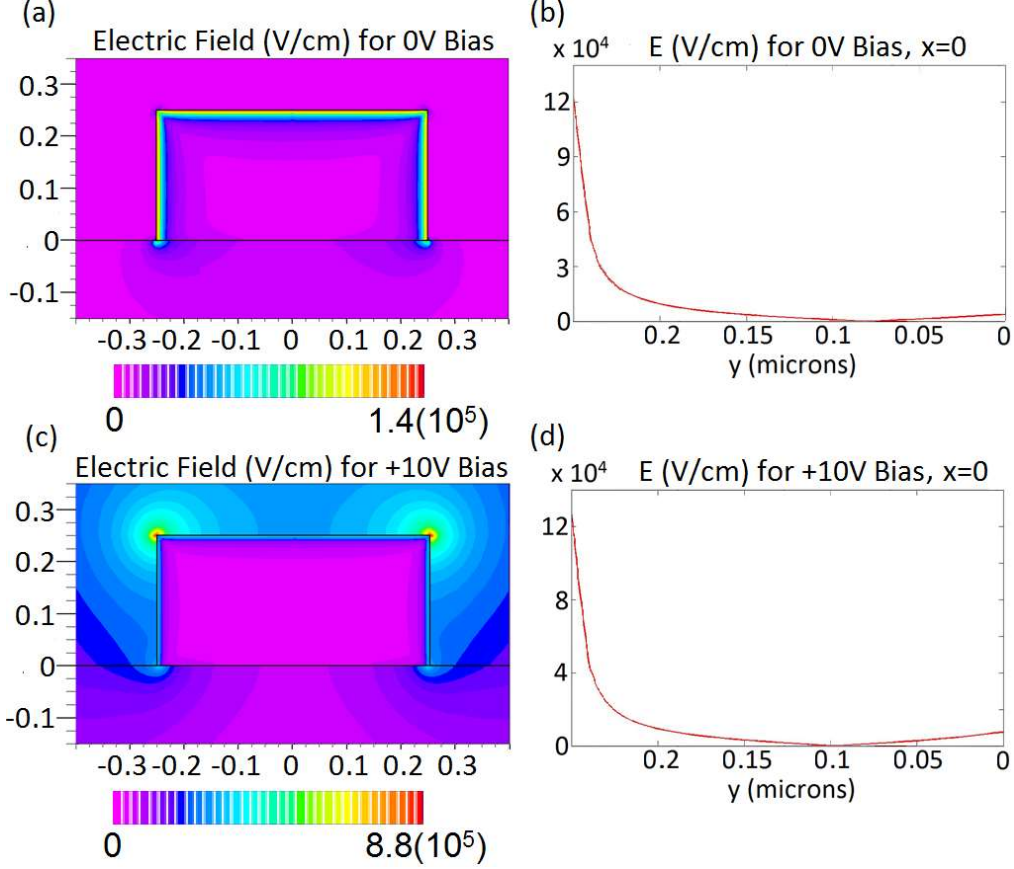
Figure. 2.3. The electric field distribution within a silicon waveguide, assuming vertical bias voltages of either 0 V (above) or +10 V (below), when the cladding material is silicon nitride. The spatial dimensions are indicated in units of microns.

2.3.2 LUMERICAL MODELLING FOR CHANGE IN EFFECTIVE INDICES

Following this result, we also investigate the effect of free carriers in silicon on the optical properties of the same set of waveguides. The free-carrier concentrations were translated to spatially dependent deviations away from the unperturbed real and imaginary parts of silicon's index of refraction, given phenomenologically as [19]:

$$\Delta n = -5.4\left(10^{-22}cm^3\right)\Delta N_e^{1.011} - 1.53\left(10^{-18}cm^3\right)\Delta N_h^{.838} \tag{2.3.a}$$

$$\Delta\alpha = 8.88\left(10^{-21}cm^2\right)\Delta N_e^{1.167} + 5.84\left(10^{-20}cm^2\right)\Delta N_h^{1.109} \tag{2.3b}$$

14

where ΔN_e is the perturbation in the concentration of free electrons and ΔN_h is the corresponding value for holes. We then used the modified values of refractive index with our FDTD solver, the multi-physics software Lumerical, to observe the effect of the carriers on the supported modes of the silicon waveguides [20]. Note that this entire analysis was performed assuming an optical wavelength of 1.55 μm. Our results for both the fundamental TE- and TM-like modes are shown in Fig. 4a-4c. It is evident that the changes in the complex effective index due to plasma dispersion are different for each of the three dielectrics. Aluminum oxide, for example, exhibits deviations in the real part of the effective index as large as 2×10^{-5} for a 10 V bias, whereas the effect is much smaller in waveguides clad with silicon dioxide. It is also interesting to note that, for each effect, the slope of the curve is opposite in sign for the waveguide clad with aluminum oxide, due to the negative value of the cladding's fixed charge.
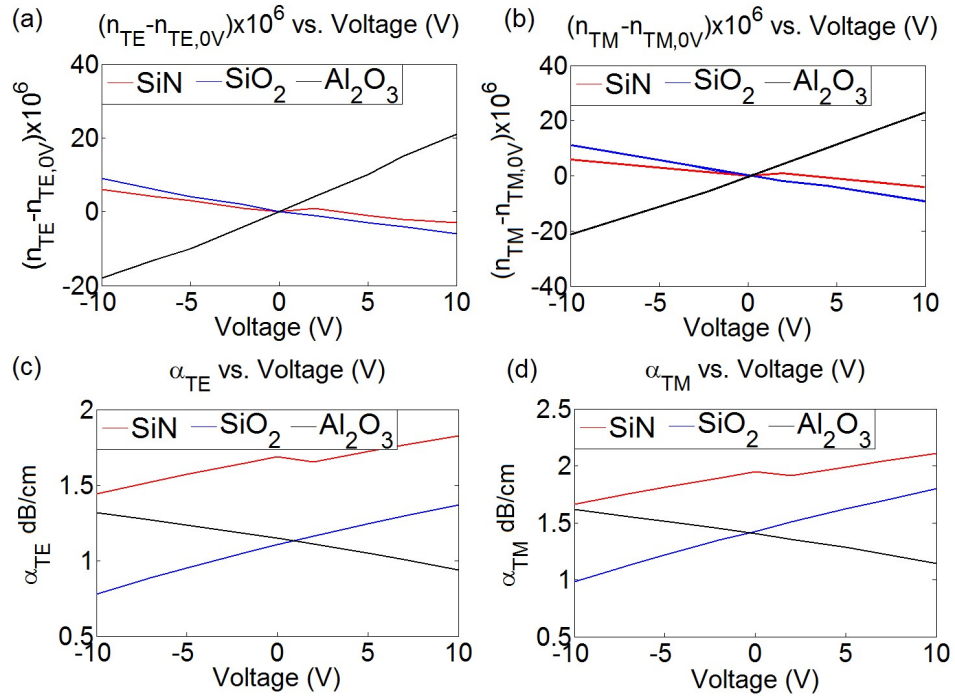
Figure. 2.4. Voltage-dependent changes in the real and imaginary parts of the effective index for the TE- (a,c) and TM-like (b, d) modes, respectively.

The net attenuation of the optical mode is dependent not only on the changes in carrier concentration, but also on the extent to which the areas of change overlap with the electromagnetic fields

of the mode itself. We hypothesis that because the optical mode supported by the waveguide clad with silicon nitride is highly asymmetric as compared to the other cases, the complex relationship between the optical mode and the free carriers is nonlinear in nature, leading to the observed kink in the plots of its parameters.

2.4 CONCLUSION

In conclusion, we have shown that silicon waveguides with dielectric claddings exhibit strong spatial deviations in carrier concentration, even in the absence of capacitively applied bias voltages, and that these changes affect the real and imaginary parts of the effective indices of the guided modes. Additionally, we have shown that the same free-carrier effects impact the waveguides' apparent electro-optic effects in response to driving voltages, both because of the changes in local carrier concentration and because of the effects the carriers have on the electric field ultimately induced across the waveguide. We stress that the purpose of this work is to demonstrate a means by which capacitive free-carrier effects may be approximately quantified in silicon waveguides. The changes in effective index shown here are comparable in magnitude to those seen in strained silicon waveguides, but because no optical devices were experimentally characterized, we cannot at this point comment on the nonlinear optical properties of strained silicon. In future research efforts, however, we are confident that the characterization method demonstrated here may be explored as a tool for decoupling the nonlinear effects present in such materials. We assert that these free-carrier effects are important to be taken into consideration in the characterization of both active and passive device components based on silicon waveguides.

Chapter 2, in part, contains materials from "Characterizing the effects of free carriers in fully etched, dielectric-clad silicon waveguides", published in Applied Physics Letters. This paper was co-authored by Matthew W. Puckett, Hung-Hsi Lin, Felipe Vallini and Yeshaiahu Fainman. The dissertation author was the first author of the manuscript.

Chapter 3

Electro-optic characterization of dielectric clad silicon ring-resonators

3.1 Background

In the following, we verify previous theoretical results which highlight the sensitivity of the capacitively-induced free carrier effect to the material used to clad a silicon waveguide. By measuring the voltage dependence of the optical properties of silicon ring resonators coupled to bus waveguides, we show that the densities of fixed charges at semiconductor-dielectric interfaces play a dominant role in determining how the waveguides' optical properties respond to bias voltages. Based on the observed electro-optic behavior, we assert that capacitively-induced free-carrier effects may be used to realize higher-efficiency optical modulators and wavemixers than what has been demonstrated to date. Furthermore, we highlight that the high density of interface charges, intrinsic to the deposition of certain claddings, result in a significant increase in the passive loss of silicon waveguides, an effect which must be considered in addition to the commonly reported sidewall roughness-induced scattering [1].

In our past work [2], we modeled the effects of free carriers in silicon waveguides clad with either silicon dioxide, silicon nitride, or aluminum oxide using the semiconductor physics tool Silvaco in combination with the finite-difference time-domain solver Lumerical [3,4]. We found that the real and imaginary parts of the TE-like mode's effective index changed differently with bias voltages for each case, and were most sensitive to the voltage for the case of aluminum oxide. This was determined to be due to the material's high negative fixed charge density at the silicon interface, which drove the semiconductor waveguide into accumulation. We additionally observed that the electric field within the silicon waveguide varied away from its unbiased value only minutely in response to applied voltages, disabling modulation

based on the Pockels effect [2]. To confirm that this behavior exists in reality, we fabricated silicon waveguides clad with silicon dioxide, silicon nitride, and aluminum oxide, then characterized the waveguides' electro-optic behavior by applying vertical bias voltages across ring resonators coupled to bus waveguides and characterizing their transmission spectra.

3.2 Fabrication

To fabricate our waveguides, we began with three silicon-on-insulator (SOI) wafers consisting of a 250 nm-thick device layer and a 3 µm-thick buried oxide layer. We spin-coated hydrogen silsesquioxane (HSQ) onto our wafers, then exposed them to patterns corresponding to our waveguides using a Vistec EBPG 5200 electron-beam lithography system with a dose of 3500 µC/cm^2. The uncovered silicon device layer was then removed using an Oxford Plasmalab 100 Reactive Ion Etcher. After etching, the wafers were submerged for 10 seconds in a 1:10 buffered oxide etchant (BOE) solution to remove the remaining HSQ from the waveguides [5]. This step was critical because baked HSQ acts as a low-quality dielectric, the presence of which can reduce the reproducibility and reliability of electro-optic measurements [6]. Overhead views of the resulting ring resonators and bus waveguides are shown in Fig. 1.
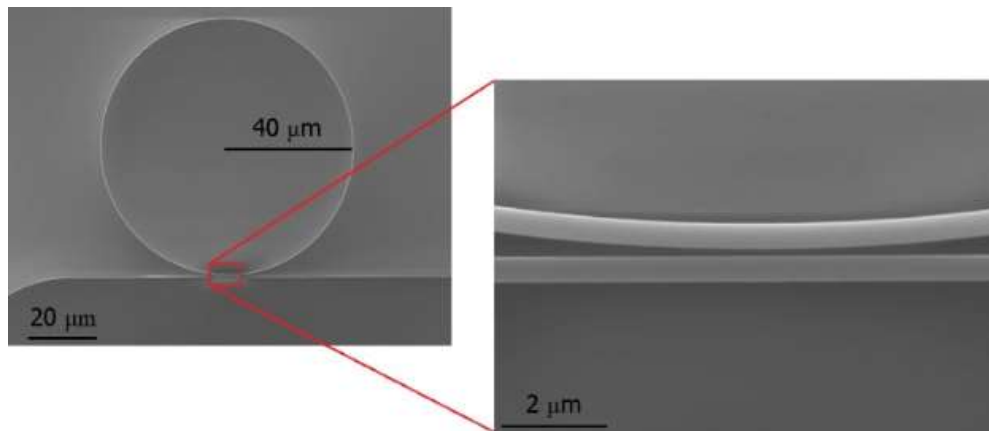
Figure. 3.1. SEM micrographs showing an unclad silicon ring resonator coupled to a bus waveguide. The ring radius is 40 µm, the waveguide width is 500 nm, and the separation between the bus waveguide and the ring is 100 nm.

One of the three samples was then clad with 50 nm of silicon nitride using an Oxford Plasmalab 100 Plasma-Enhanced Chemical Vapor Depositor (PECVD), whereas a second was clad with 50 nm of aluminum oxide using a Beneq TFS200 Atomic Layer Depositor (ALD). The resulting waveguide cross-section is shown for the silicon nitride case in Fig. 2a. Such thin layers of silicon nitride and aluminum oxide changed the electrical properties of the semiconductor-dielectric interfaces without dramatically altering the waveguides' linear optical properties. To improve the film quality and reduce the density of interface traps, a rapid thermal anneal (RTA) was carried out for both the silicon nitride and aluminum oxide wafers for 15 minutes at a temperature of 300ºC in a forming gas ambient (N_2/H_2:90%:10%) [23]. A 1.5 μm-thick silicon dioxide cladding layer was then deposited on all three samples, again using PECVD, and the RTA was repeated. The resulting TE-like optical mode supported by the silicon nitride clad waveguide is shown for example in Fig. 2b. It is important to note that the magnitude of the fixed charge at the semiconductor-dielectric interfaces, and hence the nature of the electro-optic effect, may be controlled in the future for any cladding layer by modifying either the deposition conditions, the annealing conditions, or the wafer pretreatments [7,8]. After the fabrication of the waveguides was complete, photolithography was carried out to create aluminum electrodes above the ring resonators, and the samples were finally diced to allow butt-coupling.

It is important to note that none of the cladding layers used in this work contained appreciable stress, further invalidating the strain-induced nonlinearity as a possible source of the observed electro-optic effects. The stresses contained within the aluminum oxide, silicon nitride, and silicon dioxide cladding layers were measured using a Toho Technology FLX-2320 Thin Film Stress Measurement System to be approximately 200 MPa, -300 MPa, and 200 MPa, respectively, and these values are nearly an order of magnitude smaller than those used to fabricate strained silicon waveguides [9-14].

3.3 Electro-optic modelling using SILVACO and LUMERICAL

As in past work, we used Silvaco to model the electrical properties of our three waveguides, using previously reported values for the fixed charge and interface trap densities characteristic of each cladding material [2] including a value of $4(10^{10})$ cm^{-2} for the fixed charge at the silicon/buried oxide interface. In these models, the doping of the silicon device layer was set to p-type, assuming a boron dopant concentration of 10^{15} cm^{-3}. Additionally, the bottom electrode of the simulation was placed directly beneath the buried oxide layer as in [2], although in practice the voltage would be applied to the wafer's silicon handle. This assumption is known to be valid because only a small, effectively constant voltage drop occurs across the silicon handle when this mode of voltage application is employed [11-14]. As shown in Fig. 2c and 2d, we confirmed for the case of the silicon nitride cladding that the electric field changes only marginally within the waveguide in response to bias voltages, and this eliminates the possibility of any appreciable strain-induced Pockels effect occurring.
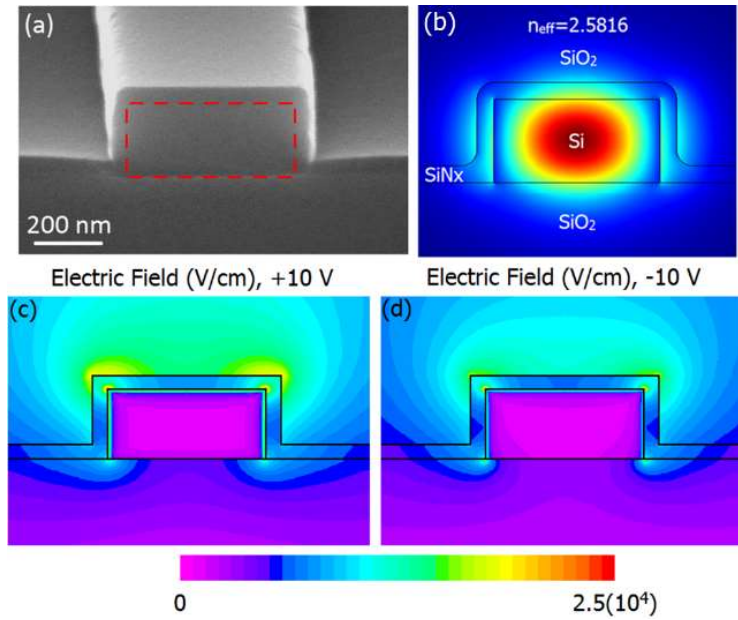
Figure. 3.2. (a) SEM micrograph of a 500 nm-wide, 250 nm-tall silicon waveguide (red dashed line) clad with 50 nm of silicon nitride. (b) The supported TE-like mode at λ=1.55 μm for the same silicon waveguide. (c,d) The magnitude of the bias electric field in V/cm across the same waveguide for (c) positive 10 V and (d) negative 10 V.

We generated voltage-dependent maps of the electron and hole concentrations within the waveguides, then translated these values through the Soref and Bennet equations into local changes in silicon's index of refraction [15]. It should be noted that these equations can be used to accurately model index changes due to capacitively induced charges for electric fields less than 10^6 V/cm [16]. By combining these results with Lumerical, we were able to predict how the effective indices of the waveguides' TE-like modes changed with voltage. Our results, shown in Fig. 3, are in agreement with those reported previously [17], showing that the slopes of both the real and imaginary index curves change sign for the case of aluminum oxide in comparison to the silicon nitride and silicon dioxide cases. Whereas the positive fixed charges present in the cases of silicon dioxide and silicon nitride drive p-type silicon into inversion, aluminum oxide's negative fixed charges have the opposite effect, inducing band bending in the opposite direction and leading to accumulation.
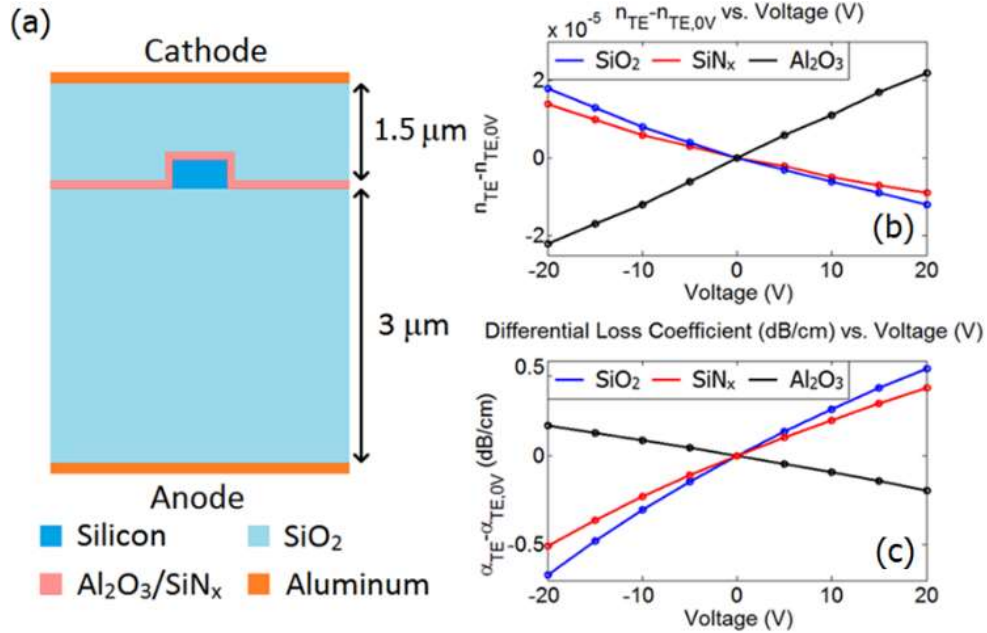
Figure. 3.3. (a) Simulated structure. (b,c) Theoretical electro-optic characteristics in terms of (b) the effective index (n_{TE}) and (c) the loss coefficient (α_{TE}) for silicon waveguides clad with either SiO$_2$ (blue), SiN$_x$ (red), or Al$_2$O$_3$ (black).

3.4 Electro-optic characterization

To measure these effects in our waveguides, we employed the optical setup shown in Fig. 4a. A tunable infrared laser was coupled into our samples at a horizontal (TE) polarization using a lensed tapered fiber. The light emitted from the samples was then collected with a metallic output objective, and the optical mode was magnified using two 4F systems of lenses. The transmitted light was then measured using an optical power meter. To apply a bias voltage across our samples, we touched probe tips to both the aluminum electrodes and the aluminum plate on which the samples were mounted, then connected the probes to a power source. This voltage application method is illustrated in Fig. 4b.
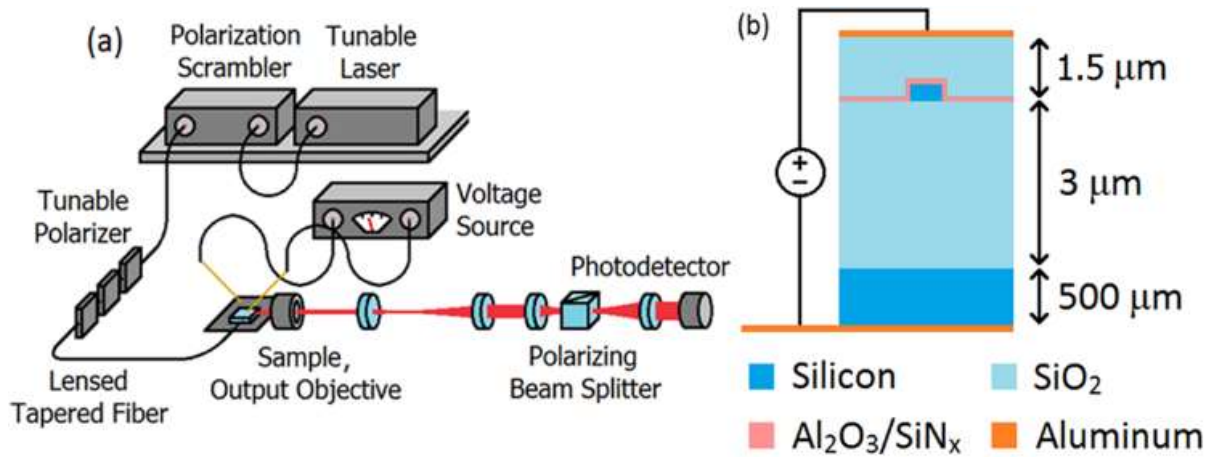
Figure. 3.4. (a) Illustration of the experimental setup used to characterize the electro-optic properties of our fabricated waveguides. (b) Cross-section of the voltage application method.

The transmission spectra we measured exhibited periodic dips at each of the rings' resonant wavelengths, and the shapes and positions of these dips could be fit to Lorentzian curves in order to extract the waveguides' loss coefficients and refractive indices. Specifically, the resonant transmission dip could be fit to the expression [18]:

$$T = \frac{t^2 - 2t\tau\cos(\theta) + \tau^2}{1 - 2t\tau\cos(\theta) + (t\tau)^2}$$

(1)

22

where t is the self-coupling coefficient of the bus waveguide, τ is the single-pass attenuation in the field including both propagation and coupling losses, and θ is the single-pass phase shift, in turn defined as [18]:

$$\theta = \frac{4\pi^2}{\lambda} n_{eff} r \qquad (2)$$

where n_{eff} is the effective index of the waveguide mode, r is the ring radius, and λ is the optical wavelength. Once the value of τ was obtained from the numerical fit, it could be used to derive the loss coefficient, neglecting the comparatively small coupling loss, as [19]:

$$\alpha = \frac{20 \log_{10}(\tau)}{2\pi r} \qquad (3)$$

Additionally, the change in the real part of the mode's effective index induced by the application of the bias voltage could be calculated from the spectral shift of the optical resonance as [18]:

$$\Delta n_{eff} = \frac{\Delta \lambda_{res}}{\lambda_{res}} n_g \qquad (4)$$

where $\Delta\lambda_{res}$ is the observed change in the central wavelength of the resonance and n_g is the group index at the resonant wavelength, extracted experimentally as [18]:

$$n_g = \frac{\lambda^2}{FSR(2\pi r)} \qquad (5)$$

In this last expression, FSR is the free spectral range of the resonances. Fig. 5a through 5c show single resonances for the three samples, and the passive loss coefficients extracted from these data were 11.3, 9.3, and 9.9 dB/cm, respectively. Loss coefficients on the order of 10 dB/cm are typical for passive waveguides of comparable dimensions which have not undergone post-etch treatments [1] and were admissible for the purposes of this study. Fig. 5d shows the voltage-dependent transmission spectra for the case of the silicon dioxide cladding. Finally, Fig. 6a and 6b summarize the results of the electro-optic

measurements, plotting the changes in both the real part of the effective index and the loss coefficient. The effects measured here are not exclusive to silicon, but have nonetheless been neglected in the electro-optic analysis of other semiconductor waveguides [20].

In a recent work [21], additional loss due to surface carrier absorption (SCA) has been characterized. In the measurements shown here, the optical power propagating through the bus waveguides was no larger than -30 dBm, and the field enhancements (FE) at the resonant wavelengths of the rings were calculated to be no greater than 5 [22], corresponding to propagating powers in the ring resonator of -16 dBm at most. This ensured that the changes in the waveguides' effective indices from SCA was orders of magnitude lower than those due to free carriers. At power levels approaching 0 dBm, however, SCA can lead to loss as large as 0.04 dB/cm and should certainly be taken into consideration [21].

The obtained results generally agree with the theoretically produced values, although the magnitudes of the both the electro-refractive and electro-absorptive effects were larger than predicted. This is potentially due to inaccuracies in the values of the fixed charge of the fabricated samples, resulting from the unique processing steps the silicon waveguides' surfaces were subjected to prior to the claddings' deposition. This discrepancy may additionally have arisen from uncertainties in (1) the interface trap density at the silicon-dielectric interfaces, (2) the index of refraction of the cladding layers, or (3) the dissimilar values of fixed charge between the upper wall and the sidewalls of the silicon waveguide, due to the different set of processes and cleaning steps they were subjected to. Lastly, silicon nitride films deposited on silicon have previously been shown to possess values of fixed charge which change in response to applied bias voltages, and this nonideality might explain why the electro-refractive response for the nitride clad waveguides was particularly large [23]. The overall trend nonetheless holds between theory and experiment, and the aforementioned uncertainties change only the magnitude of the measured effect,

not its sign. Most notably, both the electro-optic effects change direction for the case of Al_2O_3, due to its negative fixed charge, confirming that the effects seen here are due to free-carrier dispersion.
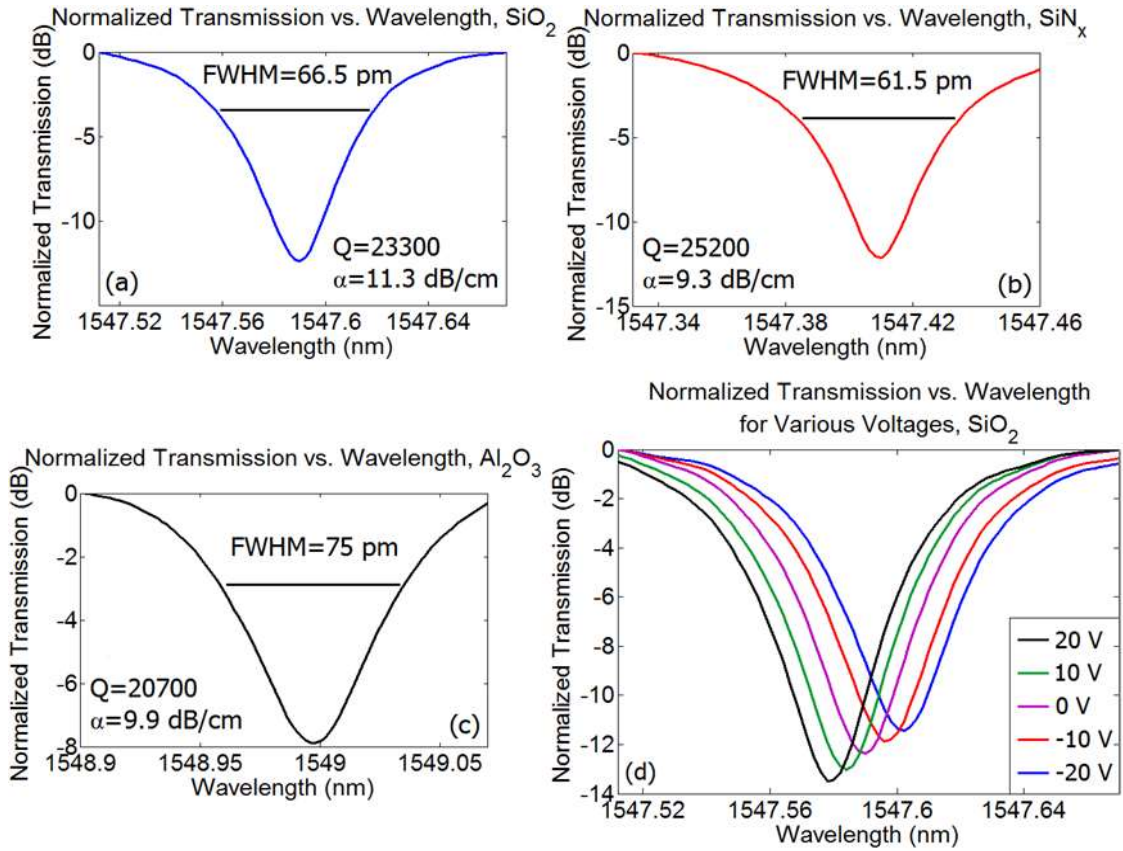
Figure. 3.5. (a-c) Passive transmission spectra showing single resonances for ring resonators in (a) SiO_2, (b) SiN_x, and (c) Al_2O_3 clad waveguides. (d) Voltage-dependent transmission spectra for the SiO_2 cladding.

Although the voltages required to characterize the present devices were large, there are several techniques, such as the use of SOI wafers with thinner buried oxide layers, which allow for them to be reduced. Most promisingly, it is possible to switch to a rib waveguide topology in which the silicon device layer itself serves as the grounding layer, and this is expected to yield a large enhancement to the electro-optic effect.
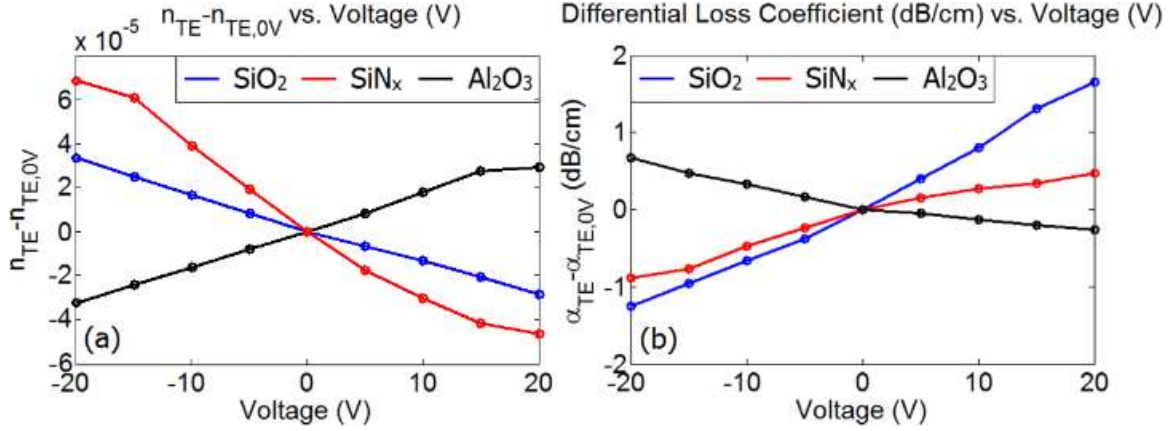
Figure. 3.6. Electro-optic characteristics in terms of (a) the effective index (n_{TE}) and (b) the loss coefficient (α_{TE}) for waveguides clad with either SiO_2 (blue), SiN_x (red), or Al_2O_3 (black).

3.5 Conclusion

In conclusion, we have shown how different dielectric claddings impact the capacitively-induced electro-optic effect in silicon waveguides. These results are significant because they clearly indicate how the capacitively-induced free-carrier effect may, in waveguides with properly chosen cladding materials, be leveraged to realize CMOS-compatible electro-optic modulators and wavemixers which do not rely on the injection of electrical currents. Additionally, this work demonstrates that a dielectric-clad silicon waveguide's optical loss may be reduced or increased by applying an appropriately chosen bias voltage, allowing for the in-vivo tuning and optimization of a wide variety of photonic devices.

Chapter 3, in part, contains materials from ""Effect of dielectric claddings on the electro-optic behavior of silicon waveguides", published in Optics Letters and co-authored by M.W. Puckett, H. Lin, A. Isichenko, F. Vallini, and Y. Fainman. The dissertation author was the first author of the manuscript.

Chapter 4

Anomalous bulk second-order nonlinearties in PECVD deposited silicon nitride thin-films

4.1 Background

The realization of a CMOS-compatible platform exhibiting large optical nonlinearities with low loss in the telecommunication optical frequency regime is of great interest in the design of highly efficient modulators, switches, and wavemixers. Silicon has long been the material of choice for integrated photonics due to its prevalence in the electronics industry [1], its transparency in the near-IR wavelength regime [2], and its high third-order nonlinear susceptibility [3], but it suffers from two-photon absorption, limiting its efficiency in nonlinear wavemixing applications [4]. Moreover, silicon's centrosymmetry causes it to lack a second-order nonlinear susceptibility, disallowing efficient and linear modulation based on the Pockels effect, as well as any sort of second-order wavemixing [5]. A substantial body of research has focused on circumventing or removing this shortcoming [6-9], but in more recent years, silicon nitride has emerged as a competing material platform, boasting a wider transparency window, no two-photon absorption, and an improved ease and flexibility of fabrication [10-14].

Silicon nitride is an amorphous material, and is not conventionally expected to exhibit any second-order nonlinearity. In free space measurements, however, silicon nitride thin films have been shown to exhibit second-harmonic generation arising from bulk nonlinearities [15]. Only an extremely small coefficient has been measured in an integrated platform to date, however, and this was attributed to interface nonlinearities [16]. If silicon nitride is to become a feasible replacement for silicon, it will be necessary for it to exhibit stronger electro-optic and wavemixing effects in a waveguide configuration than what has been shown until now.

In this chapter, we report on the first experimental measurement of a bulk second-order susceptibility in silicon nitride shown through both thin film free-space measurements and on-chip, phase-matched second-harmonic generation. In the latter case, phase-matching is achieved through dispersion engineering of the waveguides' supported modes, and the powers contained at the second-harmonic wavelengths are used to determine two of the waveguides' second-order nonlinear coefficients, $\chi_{yyy}^{(2)}$ and $\chi_{xxy}^{(2)}$. We additionally demonstrate how, by applying large bias fields across our waveguides, we may modify their second-order nonlinearities through the well-known electric field-induced second-harmonic effect (EFISH). This effect is determined to have potential for the future design of highly nonlinear silicon/silicon nitride hybrid waveguides. The results shown here not only improve the understanding of silicon nitride's role in CMOS-compatible integrated photonics, but also suggest its viability for the practical realization of optical devices which rely on appreciable second- and third-order susceptibilities.

4.2 Second-Harmonic Generation in Silicon Nitride Thin Films

Prior to fabricating waveguides, we conducted transmittance second-harmonic generation measurements via the Maker fringes method to verify the existence of nonzero second-order nonlinear coefficients in silicon nitride thin films [15,17]. We deposited varying thicknesses of silicon nitride onto a fused silica substrate using an Oxford Plasma-Enhanced Chemical Vapor Depositor (PECVD), and during the deposition process, the flow rates of the three precursor gases, SiH_4, NH_3, and N_2, were maintained at 276, 24, and 600 sccm, respectively. Four samples were fabricated with silicon nitride thicknesses ranging from 100 nm to 500 nm in order to characterize the dependence of the generated second-harmonic signal on film thickness. We focused a pulsed Ti:Sapphire laser with a pulse duration of 150 fs, a repetition rate of 80 MHz, and an average power of 100 mW at a wavelength of 800 nm onto our thin films, which were tilted at an angle of

45 degrees with respect to the normal of the incident beam. A half-wave plate was used to control the polarization of the input pump beam, and the generated second-harmonic signal at 400 nm was measured using a sequence of filters chosen to provide an OD of 12 for the pump wavelength, as illustrated in Fig. 1(a). The measured s- and p-polarized second-harmonic signals are plotted as a function of the pump polarization in Fig. 1(b) for both 200 and 500 nm-thick films. It should be noted that a bare fused silica substrate was measured as well and was found to generate no second-harmonic signal. Fig. 1(c) confirms that the measured signal is a result of second-harmonic generation by plotting its quadratic dependence on pump power.
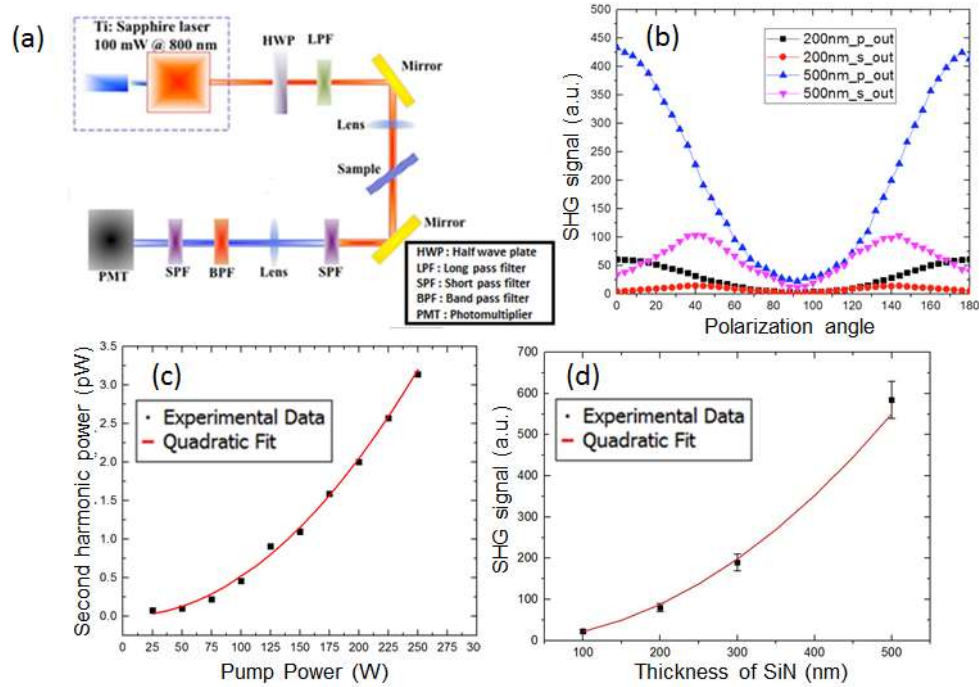
Figure. 4.1. (a) Schematic of the Maker fringe setup employed in this work. (b) Measured second-harmonic signal as a function of the pump polarization angle for s- and p-polarized input pump beams, and for 200 and 500 nm-thick nitride films. (c) Power in the second harmonic signal vs pump power exhibiting a quadratic trend (d) Normalized intensity of the p-polarized second-harmonic signal (in terms of counts in the PMT) as a function of nitride film thickness, exhibiting a clear quadratic trend.

Furthermore, it is a well-studied property of thin film second-harmonic generation that, if a second-harmonic signal is observed, its dependence on the film thickness may be used to establish the basic nature of the film's nonlinear properties. If the film lacks a second-order

susceptibility, the signal will only be generated along material interfaces where symmetry is broken, and the power contained in the second-harmonic will not vary with film thickness. If, however, the film material possesses a nonzero bulk second-order nonlinearity, the signal will vary with the square of the thickness as [15]:

$$P_{SH} \propto t_{film}^2 \qquad (1)$$

This quadratic dependence was observed, as shown in Fig. 1(d), confirming the existence of a bulk nonlinearity with potential for implementation in an integrated platform. The second-harmonic signals measured in the samples were used to calculate two different components of the $\chi^{(2)}$ tensor, $\chi^{(2)}_{yyy}$ and $\chi^{(2)}_{xxy}$, assuming that silicon nitride is of the $C_{\infty,v}$ symmetry class [15] and using a modified formulation of the maker fringes method [17]. The nonlinear coefficients were measured by fitting the experimental data to the following expressions:

$$d_{eff}^p = -d_{15}\cos(\theta_2)\sin(2\theta_1)\sin^2(\varphi') - d_{31}\sin(\theta_2)\left(\cos^2(\theta_1)\sin^2(\varphi') + \cos^2(\varphi')\right)$$
$$-d_{33}\sin(\theta_2)\sin^2(\theta_1)\sin^2(\varphi') \qquad (2)$$

$$d_{eff}^s = -d_{15}\sin(\theta_1)\sin(2\varphi') \qquad (3)$$

where d_{eff}^s and d_{eff}^p are the effective nonlinear coefficients measured for s- and p-polarized outputs, respectively, d_{15}, d_{31}, and d_{33} are the material nonlinear coefficients defined as half of their corresponding $\chi^{(2)}$ values, and θ_1, θ_2, and φ' are the two sample tilt angles and the pump polarization angle, respectively. The values this treatment yielded are tabulated below wherein the coefficients calculated for different film thicknesses are found to be in very good agreement with each other, confirming the accuracy of the employed method.

Table 4.1. $\chi^{(2)}$ calculated from the Maker fringes method

$\chi^{(2)}$ (pm/V)	100 nm	200 nm	500 nm
$\chi^{(2)}_{yyy}$	2.08±0.34	1.87±0.26	2.38±0.19
$\chi^{(2)}_{xxy}$	0.32±0.11	0.28±0.12	0.40±0.16

4.3 Modal dispersion-based phase-matching for SHG in SiN$_x$ waveguides

If we assume that the guiding material of an optical waveguide has a nonzero second-order nonlinear susceptibily, the next issue to be considered in the context of wavemixing is that of phase-matching. At every position along the waveguide's propagation length, the local second-harmonic component of the nonlinear optical polarization will give rise to an electromagnetic wavelet, and the total generated second-harmonic power measured at the output of the waveguide may be considered as a superposition of these wavelets. When the effective indices of the pump and second-harmonic modes are equal to one another, the phase mismatch vanishes and the waveletes emerging at the waveguide's output interfere coherently, leading to a large power in the second-harmonic mode. A separate type of phase-matching can also occur if the average of the effective indices of two separate pump modes equals that of the second-harmonic [18]. For nonzero values of phase mismatch, the second-harmonic power generated in a waveguide is a sinusoid with respect to the propagation length, whereas when the phase mismatch equals zero, it increases monotonically.

There are several methods which may be employed to achieve phase-matching. In this work we choose to modify the waveguide cross-section, leveraging its geometric anisotropy to control the effective indices of its supported modes. Let us assume a pump wavelength of 1550

nm, a corresponding second-harmonic wavelength of 775 nm, a waveguide height of 550 nm, and a sidewall angle of 83º. These values have been chosen because they correspond to fabrication results which will be shown subsequently. Using a finite element method (FEM) software such as Comsol, we may predict how the effective indices of the waveguides' supported modes change with the base waveguide width [19]. The refractive index of our nitride layer was measured through ellipsometry to be 2.01 at the second-harmonic wavelength, and a value of 1.99 at the pump wavelength is taken from our previous work [10]. As shown in Fig. 2(a), phase-matching may theoretically be attained via different components of the $\chi^{(2)}$ tensor between either (1) the TM-like pump mode and the TE- or TM-like second-harmonic mode, or (2) the combined TE- and TM-like pump modes and the TE- or TM-like second-harmonic mode. Two intersections, indicated in Fig. 2(a) with dashed black lines, are of particular interest because they rely on the two $\chi^{(2)}$ tensor components which were shown in the previous section to be nonzero in silicon nitride thin films. The profiles of the second-harmonic modes of interest are shown for reference in Figs. 2(b) and 2(c).
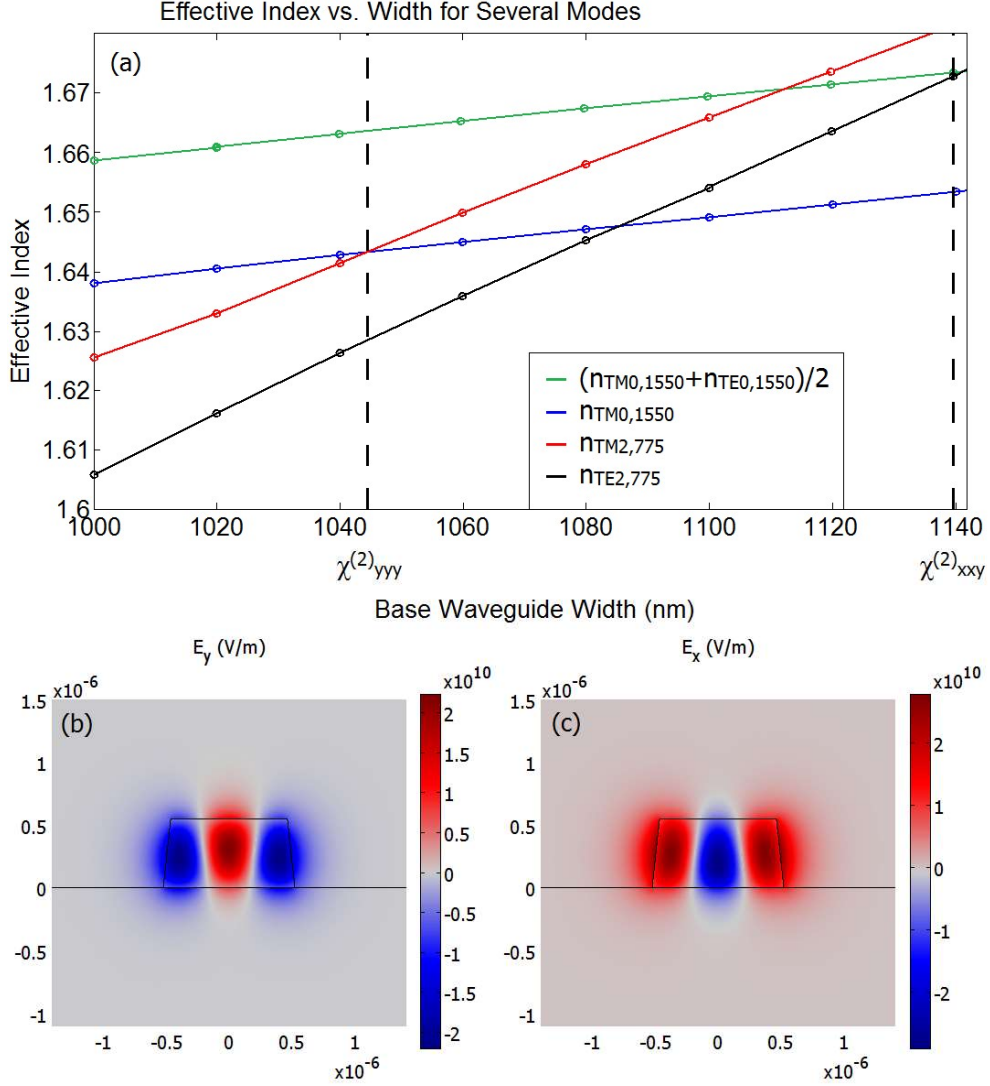
Figure. 4.2. (a) Effective indices of the TM-like pump (blue) and two second-harmonic modes (red, black) as a function of the waveguide width, as well as the average effective index of the TE- and TM-like pump modes (green). Phase-matching based on nonzero nonlinear coefficients occurs at widths of approximately 1045 and 1140 nm, respectively (dashed black lines). (b-c) Arbitrarily normalized electric field profiles of the TM- and TE-like second-harmonic modes, respectively, assuming a pump wavelength of 1550 nm and a base waveguide width of 1050 nm.

Coupling into the TM-like second-harmonic mode relies on the existence of $\chi^{(2)}_{yyy}$, whereas coupling into the TE-like second-harmonic is based on $\chi^{(2)}_{xxy}$. The other two intersection points shown in Fig. 2(a) (black/blue and red/green) may be disregarded because they rely on tensor components which are believed to be identically zero [9]. Thus, by discriminating between the orthogonal polarizations of the generated second-harmonic signal at the output of the waveguide, the two nonzero nonlinear coefficients of interest may be independently characterized.

4.4 Experimental Phase-Matched Second-Harmonic Generation

4.4.1 Fabrication

Following our free-space measurements, we set out to fabricate and characterize waveguides composed of the same nitride layer. For this particular demonstration, we began our fabrication process with silicon-on-insulator (SOI) wafers consisting of 500 nm-thick device layers and 3 μm-thick buried oxide (BOX) layers. The silicon device layer was removed through submersion in a solution of 1:10 tetramethylammonium hydroxide (TMAH) heated to a temperature of 70 ºC for one minute, and following this, we deposited 550 nm of silicon nitride, again through PECVD. In the future, nitride films may be deposited on oxidized silicon wafers, removing the need to use expensive SOI wafers [14]. After this new device layer was fabricated, we spin-coated the electron-beam resist hydrogen silsesquioxane (HSQ) onto our wafers, prebaked them for two minutes at 190ºC, and exposed them through electron-beam lithography to patterns corresponding to 3.3 mm-long meandering waveguides with widths ranging from 700 nm to 1.12 μm in steps of 5 nm. This was done to ensure that, for at least one of the waveguides in our experiments, phase-matching would be achieved at a pump wavelength around 1550 nm. Following the lithographical step, the wafers were submerged for one minute in a solution of 1:4 TMAH to remove the unexposed HSQ. Next, the portion of the device layer left unprotected by HSQ was removed through reactive ion etching (RIE) in an Oxford Plasmalab 100. The waveguide cross-section which resulted from this fabrication process is shown in Fig. 3, and it is important to note that, although the base waveguide width matched the design width exactly, undercut during the etching process resulted in the waveguide width at the top being reduced by approximately 120 nm.
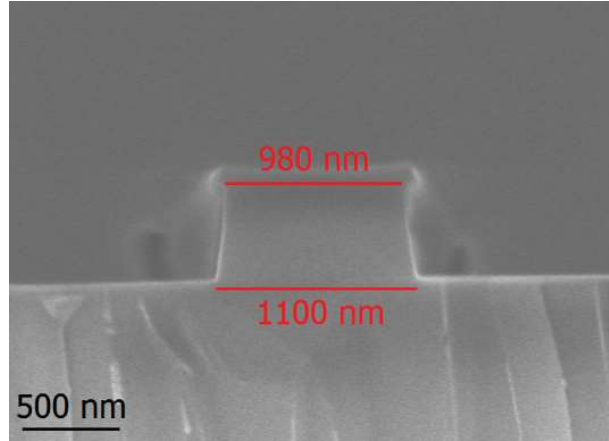
Figure. 4.3. SEM micrograph of an unclad silicon nitride waveguide, showing the slope of the sidewalls and the remaining unetched HSQ layer.

Following the etch step, the wafers were clad with 2 μm of silicon dioxide again using an Oxford Plasma-Enhanced Chemical Vapor Depositor. Finally, the samples were diced along the waveguide edges to allow butt-coupling via a lensed tapered fiber.

4.4.2 Characterization and Results

To measure the throughput of the pump mode, as well as any power at the second-harmonic wavelength, we employed a setup used in previous work [9,20,21]. Light from a CW laser, which was tunable from 1470 to 1570 nm, was directed into a polarization scrambler, then subsequently coupled into an erbium-doped fiber amplifier (EDFA) with a maximum output power of 1.1 W. The output of the EDFA was then directed into our silicon nitride waveguides using a lensed tapered fiber, and the transmitted light, consisting of both the fundamental and second-harmonic fields, was collected using a reflective objective. The light collected by the objective was then magnified using two 4F lens systems and characterized by either (1) an IR powermeter, (2) a fiber-coupled spectrometer, or (3) shortpass filters and a visible spectrum powermeter. Additionally, free-space TE- and TM-polarizers were used to distinguish between different output polarizations.

Phase-matching into the TM-like mode was observed at a pump wavelength of approximately 1559 nm and a waveguide width of 1010 nm, corresponding to only a slight deviation of 35 nm from the theoretically predicted width, 1045 nm. Using the visible powermeter, we measured the wavelength- and power-dependent second-harmonic signal emitted by the waveguide, and the measured data sets are shown in Fig. 4(a). In addition to the expected second-harmonic signal, appreciable optical power was measured even at wavelengths away from phase-matching, and we believe this corresponds to fluorescence due to impurities and defects in the nitride film, an effect which has previously been observed in multiple integrated platforms [22,23]. Nonetheless, the power in the second-harmonic could be determined by taking the difference between the non-phase-matched power and the phase-matched value. By repeating our measurement of the second-harmonic signal for several different values of pump power, we determined that the signal scaled quadratically with the pump, as expected, whereas the photoluminescence pedestal upon which the signal sat scaled linearly. This trend, shown in Fig. 4(b), clearly indicates that the observed second-harmonic field resulted from the existence of a second-order susceptibility in silicon nitride.

The second-order nonlinear coefficient was extracted from the measured data as [18]:

$$\chi_{yyy}^{(2)} = \frac{4A_{2\omega}}{\left(\dfrac{\Gamma}{1W}\right)\omega\varepsilon_0 L A_\omega{}^2}$$

(4)

where $A_{2\omega}$ is the second-harmonic amplitude, ω is the angular frequency of the pump (rad/s), ε_0 is the permittivity of free space (F/m), L is the propagation length (m), A_ω is the pump amplitude, and Γ is the spatial overlap between the pump and second-harmonic modes within the waveguide, defined in turn as [18]:

$$\Gamma = \iint\limits_{SiN_x} E_{y,2\omega}^{*}(x,y)E_{y,\omega}^{2}(x,y)\,dxdy \tag{5}$$

where $E_{y,2\omega}$ and $E_{y,\omega}$ are the relevant electric field components of the corresponding second-harmonic and pump modes (V/m), normalized to 1 W of time-average propagating power. Again using the FEM software COMSOL, we calculated Γ to be $7.56(10^8)$ V^3/m , and this gives us a $\chi^{(2)}_{yyy}$ of 0.12 pm/V. It should be noted, however, that this treatment neglects loss within the waveguide at both the pump and second-harmonic wavelengths. The loss coefficient at 1550 nm may safely be assumed to be negligibly low (nearly 97% transmission through 3.3 mm-long samples) using loss values for our own previously reported results [10], and if we assume an upper limit for the loss coefficient at 775 nm of 100 dB/cm, corresponding to an unrealistic worst-case scenario, the obtained upper bound of $\chi^{(2)}_{yyy}$ is calculated to be 0.48 pm/V [24]. We can therefore say with confidence that the actual value of $\chi^{(2)}_{yyy}$ lies between 0.12 and 0.48 pm/V, or $\chi^{(2)}_{yyy}=0.3\pm0.18$ pm/V.

For a waveguide width of 1070 nm and a pump wavelength of 1541 nm, we additionally observed phase-matching into the TE-like second-harmonic mode from the combined TE- and TM-like pump modes. The measured second-harmonic power is plotted as a function of the pump wavelength in Fig. 4(c), and again the photoluminescence pedestal is visible away from the phase-matched wavelength. For the case of two pump modes interacting with a second-harmonic mode, Eq. (4) changes slightly to [18]:

$$\chi^{(2)}_{xxy} = \frac{2A_{2\omega}}{\left(\dfrac{\Gamma}{1W}\right)\omega\varepsilon_0 L A_{\omega,TE} A_{\omega,TM}} \tag{6}$$

where $A_{\omega,TE}$ and $A_{\omega,TM}$ are the amplitudes in the TE- and TM-like pump modes, respectively, and Γ is again the confinement factor, now defined as [18]:

$$\Gamma = \iint\limits_{SiN_x} E_{x,2\omega}{}^*(x,y)E_{y,\omega,TM}(x,y)E_{x,\omega,TE}(x,y)dxdy \qquad (7)$$

where $E_{y,\omega,TM}$ and $E_{x,\omega,TE}$ are the relevent field components of the normalized pump modes. Using a FEM-calculated value for Γ of $6.46(10^8)$ V^3/m and applying a treatment identical to that used for $\chi^{(2)}{}_{yyy}$, we determine that the value of $\chi^{(2)}{}_{xxy}$ for these waveguides is between 0.06 and 0.22 pm/V, or $\chi^{(2)}{}_{yyy}$=0.14±0.08 pm/V. The fact that our integrated measurements yield smaller coefficients than their free-space counterparts is somewhat intuitive because, as the pump wavelength moves farther away from the band edge of any dielectric material, the value of $\chi^{(2)}$ is known to be highly dispersive [25]. The observed discrepancy between the two methods may additionally be due to the fact that, during the fabrication of the waveguides, silicon nitride is subjected to chemical, mechanical, and thermal conditions which are known to cause changes in its composition [26,27]. Optimization, including changes to the deposition conditions, may likely be made in the future to produce a higher value of $\chi^{(2)}$ in the fabricated waveguides [11,15].
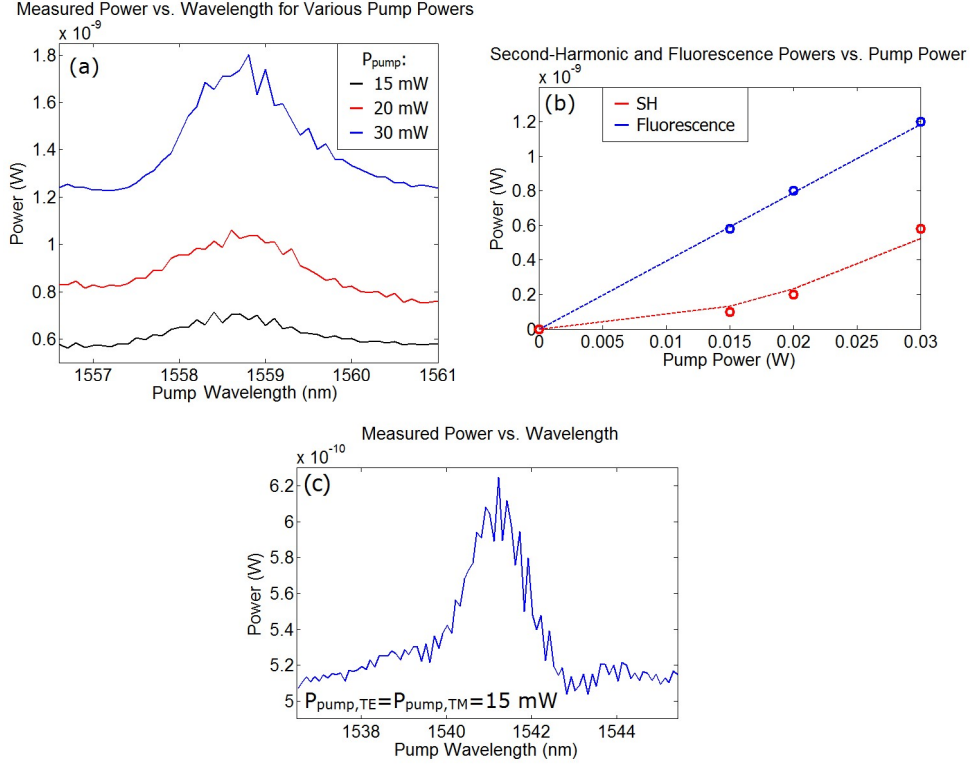
Figure. 4.4. (a) Measured TM power generated in a 1010 nm-wide silicon nitride waveguide, as a function of the pump wavelength, for several different pump powers. (b) Power dependences of the measured fluorescence background and the second-harmonic signal at the phase-matched wavelength. (c) Measured TE second-harmonic power generated in a 1070 nm-wide silicon nitride waveguide, as a function of the pump wavelength.

4.5 EFISH based enhancement in Second-Harmonic Generation

Let us assume that a static electric field exists within a third-order nonlinear material. If an electromagnetic field propagates through the same medium, the static and oscillating fields will interact to generate a third-order polarization oscillating at twice the incident frequency, given as [28]:

$$P_{2\omega} = \frac{\varepsilon_0}{2} \chi^{(3)}(0,\omega,\omega) E_{DC} E_{\omega} E_{\omega} \tag{8}$$

where E_{ω} and E_{DC} are the electromagnetic and bias fields, respectively. This effective second-order material polarization will then generate a new electromagnetic wave, and although this is in fact a third-order process, it mimics the behavior of second-order nonlinear materials. This means of

generating a second-harmonic electromagnetic wave is known as the EFISH effect mentioned previously.

In our silicon nitride waveguides, the standing electric field discussed above may be generated by depositing aluminum electrodes above our silicon dioxide cladding layers and applying a bias voltage vertically across the waveguides' cladding layers, as illustrated in Fig. 5(a). Unlike the case of semiconductor waveguides, in which free charge carriers shield external bias fields, the field inside the nitride waveguide is relatively uniform and can be as high as 10^8 V/m for an applied voltage of 500 V. As the voltage is increased, the field-induced $\chi^{(2)}_{eff}$ is anticipated to interact coherently with the silicon nitride's intrinsic $\chi^{(2)}$, allowing the material's total second-order susceptibility to be changed. Fig. 5(b) shows that the proposed fabrication has in fact been carried out, providing an SEM micrograph of the cross-section of the waveguide and electrode, and Fig. 5(c) shows the voltage dependence of the TM second-harmonic signal generated in the 1010 nm-wide waveguide, as measured in a fiber-coupled spectrometer. The fact that the phase-matched wavelength has blue shifted relative to the data shown in Fig. 4(a) highlights the significance of random variation among different fabrication runs. As illustred in Fig. 5(d), the peak count of the second-harmonic signal increases quadratically with applied voltage, and this is in good agreement with the theoretically anticipated linear increase in the second-order susceptibility. The narrow spectral shape of the signal provides additional confirmation that the measured signal is second-harmonic generation, and the measured increase in the second-harmonic power of 16-18% for an applied voltage of 500 V corresponds to a field-induced increase in silicon nitride's $\chi^{(2)}_{yyy}$ of approximately 8-9%. The magnitude of $\chi^{(3)}$ in silicon nitride, although highly variable, is typically on the order of 10^{-21} m^2/V^2 [10], and for our waveguide geometry this corresponds to a $\chi^{(2)}_{eff}$ on the order of 10^{-14} m/V when 500 V are applied vertically. Our

experimental results are therefore in good agreement with theory. Although the observed enhancement to the second-order nonlinear susceptibility is small, we assert that by using materials such as silicon-rich silicon nitride, which has a third-order nonlinear susceptibility multiple orders of magnitude greater than that of typical silicon nitride [29], EFISH may eventually be used to substantially increase the conversion efficiencies attainable by material platforms similar to the one shown here.
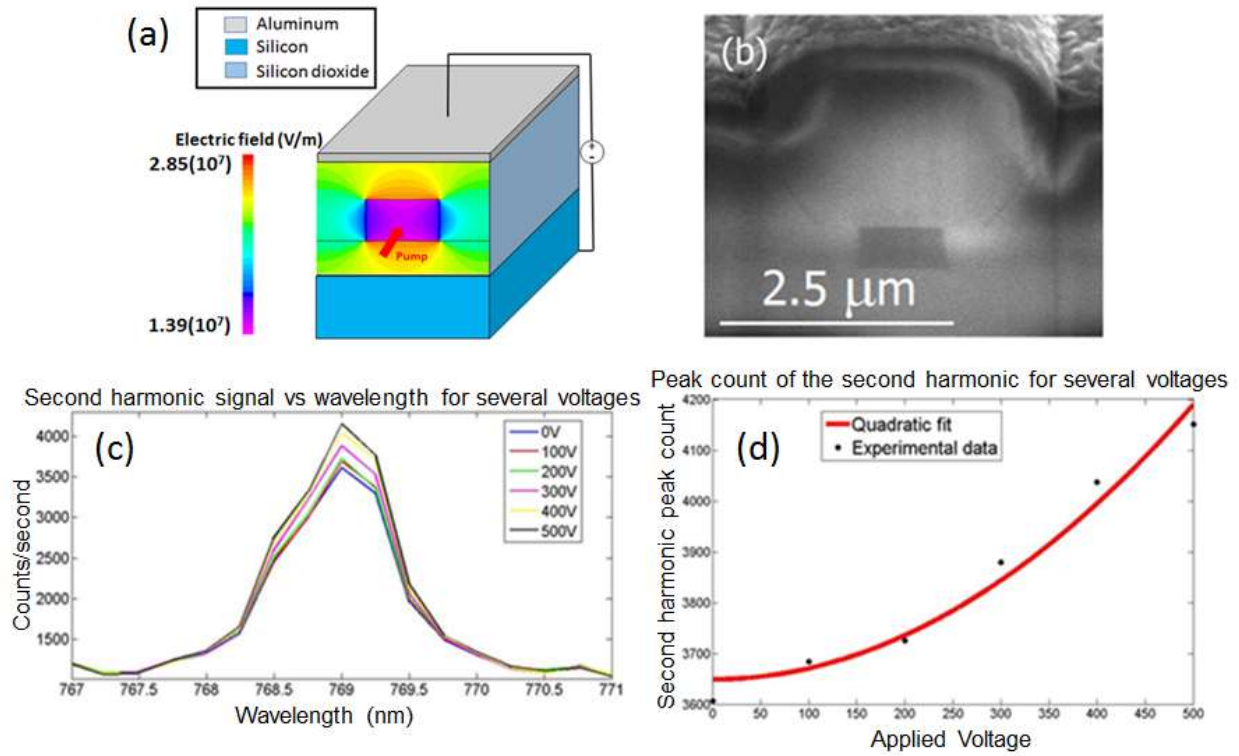
Figure. 4.5. (a) Schematic of the proposed mode of voltage application across a silicon nitride waveguide. Superimposed is the electric field simulated in SILVACO for the same structure with an applied voltage of 130 V. (b) SEM micrograph of a silicon nitride waveguide clad with layers of silicon dioxide and aluminum. (c) Spectrometer-measured second-harmonic signal, plotted as a function of wavelength, for several different bias voltages. (d) Peak count of the second-harmonic signal vs. the applied voltage, exhibiting a quadratic trend as would be expected for a linear increase in the second-order susceptibility.

4.6 Conclusion

To summarize, we have shown for the first time that the bulk second-order nonlinear susceptibilities observed in free-space measurements of silicon nitride thin films may be used in a

CMOS-compatible integrated platform to achieve second-harmonic generation which is phase-matched through dispersion engineering of the waveguide geometries. By considering the polarizations of the optical modes relevant to the wavemixing process, we characterized two specific components of the $\chi^{(2)}$ tensor, $\chi^{(2)}_{yyy}$ and $\chi^{(2)}_{xxy}$. We additionally demonstrated how the application of bias voltages across silicon nitride waveguides can lead to an effective increase in their second-order nonlinear susceptibilities and discuss how the enhancement measured here may be improved upon in future work. As new material candidates continue to be considered for the advancement of integrated photonics, we believe characterizations like the ones presented here will be critical in determining which material platform shows the most promise for the realization of a new generation of nonlinear optical devices.

Chapter 4, in part, contains materials from "Observation of second-harmonic generation in silicon nitride waveguides through bulk nonlinearities" published in Optics Express and co-authored by Matthew Puckett, Hung-Hsi Lin, Mu-Han Yang, Felipe Vallini and Yeshaiahu Fainman. The dissertation author was the first author the manuscript.

Chapter 5

Dispersion in observed second-order nonlinearity in silicon-rich-nitride

5.1 Background

There is an acute need for a highly nonlinear material that can be integrated with silicon to achieve efficient, high-speed, linear electro-optic modulation and nonlinear wave mixing [1-3]. In recent years, silicon nitride has emerged as one such promising candidate with salient features such as a wide transparency window, ease of fabrication and compatibility with silicon photonics manufacturing [4]. While traditionally silicon nitride has been seen as a centrosymmetric dielectric, lacking any second-order nonlinear susceptibility [5], recent results in literature have shown that silicon nitride can exhibit an anomalous second-order nonlinear susceptibility [6,7], the origin of which remains unclear.

While reported results have shown the second-order nonlinear properties of silicon nitride thin-films to vary across deposition techniques, and associated conditions, work in literature has not focused on the variety of wavelengths employed in these experimental studies. There have been reports in literature on thin-films of stoichiometric silicon nitride which have demonstrated a bulk second-order nonlinear susceptibility, $\chi^{(2)}$, as high as ~3pm/V, at a pump wavelength of 800nm [6,7]; while other results have utilized in-waveguide, phase-matched, second harmonic generation to report values as low as ~0.3pm/V in stoichiometric films at a pump wavelength of 1550nm [7,8]. Previously, we have attributed this discrepancy, in measured coefficients using free-space and in-waveguide measurements, to a lack of perfect phase-matching and/or modifications introduced into the materials during fabrication [7]. To the best of our knowledge there has not

been a conclusive discussion or reported results thus far on this discrepancy, and its dispersive nature, in literature.

In this chapter, we undertake a systematic evaluation of the second-order nonlinear properties exhibited by silicon nitride thin films. We discuss methods to enhance the observed $\chi^{(2)}$ by both increasing the silicon content in the films as well as through the electric-field induced second-harmonic effect (EFISH). Lastly, we also report on our observation of a high degree of dispersion in the $\chi^{(2)}$ exhibited by these films.

5.2 Silicon-rich nitride

Bulk nonlinearities in silicon nitride thin films deposited through plasma enhanced chemical vapor deposition, PECVD, and RF magnetron sputtering have been reported on in the past [6]. The first measurement of this nonlinearity using in-waveguide experiments was reported in 2016 [7], where we carried out phase-matched second-harmonic generation in stoichiometric silicon nitride waveguides. The magnitude of the reported nonlinearity was low with in-waveguide measurements (at 1550nm) yielding values of $\chi^{(2)}$ lower than 1pm/V. These values have subsequently been reproduced and confirmed in a separate measurement [8]. By leveraging a unique attribute of the silicon nitride platform, this relatively small nonlinearity can be enhanced by changing the stoichiometry of the deposited films. It is known that increasing the silicon content in sputtered silicon nitride thin films, yielding so-called silicon-rich nitride (SRN) films, leads to an enhancement in the magnitude of the third-order nonlinearity [9]. However, these films suffer from high propagation loss, making them inapplicable to many in-waveguide applications. There have been two recent reports [10,11] extending these results to PECVD deposited SRN films carried out using free-space measurements with pump wavelengths of 800nm and 1040nm

respectively. The SRN material was shown to possess an enhanced second-order nonlinearity compared to that of stoichiometric films, while its propagation loss values remained relatively low.

With an intent to evaluate these films for in-waveguide applications, we carried out a systematic study of the effect of silicon content on the exhibited linear and nonlinear optical properties of the films. Three different samples, labelled S_1, S_2, and S_3, were fabricated with silicon nitride films deposited on fused-silica substrates. The flow-rate of silane (SiH_4), one of the precursors in the PECVD process, was varied across the samples from 180, 276, and 500sccm, while keeping all the other deposition parameters (outlined in [7]) constant. Ellipsometry measurements using light at 632.8nm confirmed that this fabrication process produced films with unequal refractive indices of 1.9 (S_1), 2.08 (S_2) and 2.25 (S_3), with the index of the film scaling positively with the SiH_4 flow-rate. The reason for this was confirmed to be an increase in silicon content by carrying out electron-dispersive X-ray (EDX) spectroscopic measurements. Fig. 1a shows the composition of the films in terms of their silicon and nitride atomic percentages (shown in red and blue colors respectively), with a silicon content of 41% (S_1), 51% (S_2), and 56% (S_3) across the three films.

5.3 Free-space measurements

In order to characterize the effect of the silicon content in these films on their nonlinear properties, polarization dependent SHG experiments were carried out using a femtosecond Ti:Sapphire laser source at a wavelength of 800nm, with a pulse duration of 150fs, an 80MHz repetition rate, and 100mW of average power. The pump beam was focused using a 20X microscope objective to a focal spot on the surface of the SRN sample, with a beam waist of 50um, and a confocal parameter much longer than the thickness of the film. The generated s- and p-

polarized SHG signals were detected as a function of the polarization angle of the pump. Further details of the characterization setup can be found in the supplementary information. All of the SiN thin films were grown to the same thickness of 400nm and were deposited on 1.5cm x 1.5cm fused silica substrates. A commercial 500 μm thick X-cut quartz wafer, exhibiting a nonlinear coefficient $\chi^{(2)}_{xxx}$ of 0.64 ± 8% pm/V is used to calibrate the system, and the absolute values of $\chi^{(2)}$ tensor components from our samples are determined by comparing the generated SHG signals with those from the quartz sample under the same experimental conditions. The use of thin-films in this study helps to avoid the need for any phase-matching, including the need to account for dispersion in the linear refractive index in the silicon nitride films, while calculating the generated second-harmonic power using the revised Maker-fringes analysis [7]. For example, in the case of a 400nm thick SRN film (n=2.25 at λ_{pump}=800nm), a relatively high dispersion of up to 10^{-2} in linear refractive index from the pump to the second-harmonic wavelength (λ_{SHG}=400nm) would cause a change of only 0.04% in the calculated second-harmonic power and hence dispersion in linear refractive index can be neglected. Additionally, it should be noted that the measurement errors in this study originate mainly from the fluctuation of laser power due to the unstable humidity of environment (±5%), fluctuation of readings from PMT resulting from the influence of background noises (±20%), and the non-uniformity in the thickness of the deposited thin films (±10%). Besides, the possibility of counting error (±10%) of photons in the PMT (Hamamatsu Inc., H11461-03) due to pulse-overlapping, as described in the handbook, is also taken into account [13]. Furthermore, in order to minimize these errors, the generated SHG intensities from quartz and SiN thin films are determined by the average of five different spots on each sample. The revised Maker fringes analysis was then employed to carry out the tensorial analysis of the second-order nonlinearity [7, 11-13]. As is evident from the figure, the generated second-harmonic signal from the film with the

highest silicon content (S_3) is up to 10 times larger compared to that generated from the film with a stoichiometric composition (S_1). Additionally, these polarization dependent second-harmonic responses were then used to extract the tensorial components of the observed $\chi^{(2)}$ in these films. The extracted values of the all-normal ($\chi^{(2)}_{zzz}$) and in-plane ($\chi^{(2)}_{zxx}$) components are tabulated in Table I, and are found to be up to 3.3 times larger for the SRN film (sample S_3) when compared with the stoichiometric film (sample S_1). Furthermore, to the best of our knowledge the measured tensor component $\chi^{(2)}_{zzz}$ in the SRN film is the largest reported to-date in as-deposited PECVD silicon nitride films, and the experimental results also verify that the increasing silicon content in SiN thin films leads to enhancement in the second order nonlinear susceptibility.
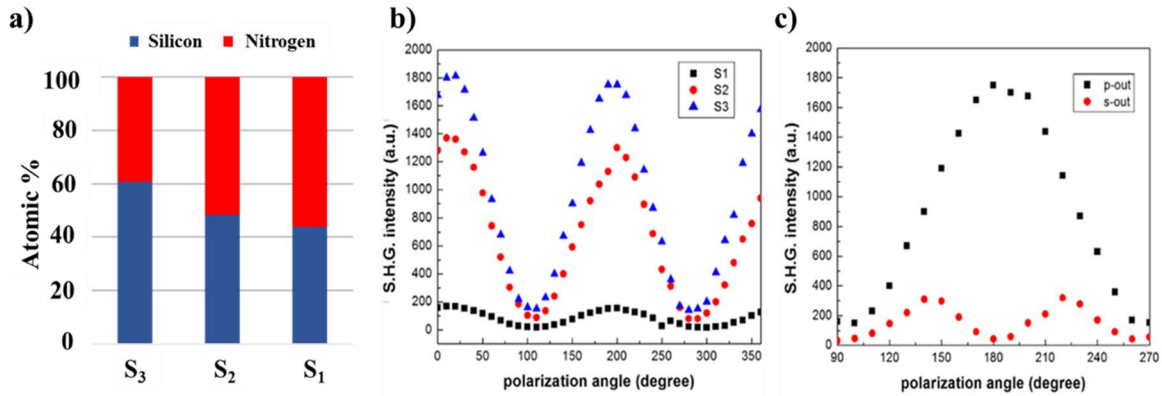

Figure. 5.1. (a) Composition of the samples, S_1, S_2, and S_3, in terms of the atomic percentages of silicon and nitrogen, extracted using EDX spectroscopy (b) Second-harmonic signals generated from the three films as a function of polarization angle for p- polarization. (c) SHG signals from the SRN film (S_3) for both s- and p-polarized input pumps.

47

Table 5.1. The deposition recipes and measured properties of silicon nitride thin films.

Sample	SiH₄ flow rate (sccm)	Si %	Refractive index (λ=632.8nm)	$\chi^{(2)}_{zzz}$ (pm/V)	$\chi^{(2)}_{zxx}$ (pm/V)
S_1	180	41	1.9	2.4	0.4
S_2	276	51	2.08	5.8	1.1
S_3	500	56	2.25	8	1.9

5.4 Electric field induced enhancement in nonlinearities

An alternative method to enhance the nonlinear response in these films is the electric-field induced second-harmonic (EFISH) effect. In our previous work [7], we presented in-waveguide results demonstrating enhancement of the second-harmonic response from silicon nitride waveguides by applying an electric field across them. It was shown then that the applied external electric field interacts with the third-order nonlinearity of the films, resulting in a higher effective second-order response, and a corresponding increase in the intensity of the second-harmonic signal from the waveguides [7]. To analyze the tunability of the nonlinear response in the SRN films, we fabricated 50nm thick films of the three silicon nitride films sandwiched between two electrodes made of 10nm thick layers of indium tin oxide (ITO) on a fused silicon substrate as shown in the schematic in Fig. 2a. The ITO films serve as the transparent electrodes across which an external DC voltage is applied while carrying out SHG experiments. It should be noted that while the ITO films were not optimized with respect to their conductance, they were still sufficient for carrying out preliminary studies on the EFISH induced tunability in the films. Fig. 2b shows the SHG response for the SRN film, with pump and second-harmonic wavelengths of 800 and 400nm respectively, as a function of the applied voltage, clearly demonstrating a wide range of tunability. The SHG response is found to increase quadratically with respect to the applied voltage, which is

in agreement with our prediction of EFISH. It should also be noted that the minimum in the measured quadratic response is found to be at a small negative bias voltage and not at zero-bias. This is because at this voltage, the artificially created second-order nonlinearity generated by the external electric field and the high $\chi^{(3)}$ coefficient of SiN perfectly negates the all-normal $\chi^{(2)}_{zzz}$ present in the as-deposited film. As a result, the magnitude of the SHG response reduces, but is still not perfectly zero because of contributions from the in-plane components of the $\chi^{(2)}$ in the as-deposited nitride film, ITO layers, as well as those arising out of any surface nonlinearities.

The SHG signal measured at an applied voltage of 8V was found to be up to 36 times larger than that measured at zero-bias. Table II summarizes the calculated highest and lowest effective $\chi^{(2)}_{zzz}$ components of three different silicon nitride samples fabricated with the same silicon contents as S_1, S_2 and S_3. The SRN film demonstrates an effective $\chi^{(2)}$ spanning from ~3pm/V to as high as 22pm/V. This relatively large range of tunability is in accordance with reports in the literature of an enhanced third-order nonlinear response in silicon-rich nitride films when compared to their stoichiometric counterparts [14-16]
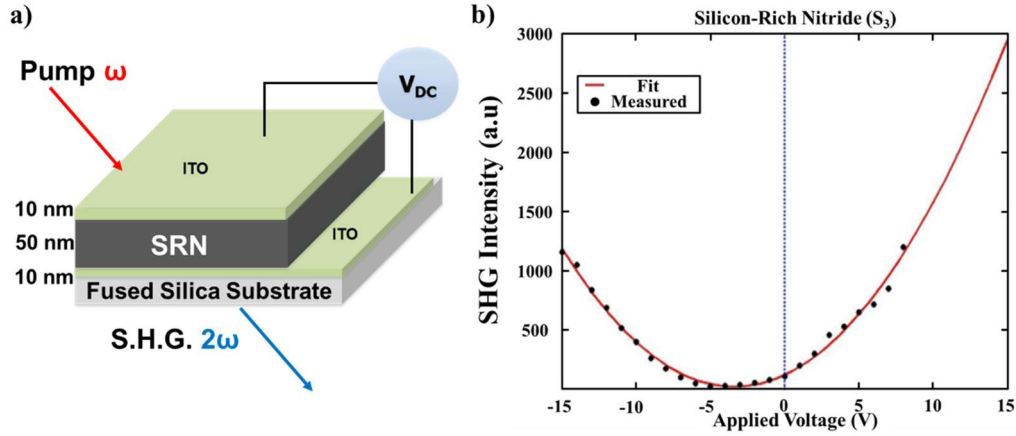
Figure. 5.2. (a) Schematic illustration of the SHG response (λ_{pump}=800nm, λ_{SHG}=400nm) from a 50nm silicon nitride film sandwiched between two 10nm ITO films on a fused silica substrate. (b) Experimental (black dots) and quadratic fitting (red) curve showing the SHG response from a SRN sample as a function of the external voltage applied across the layer.

Table 5.2. As-deposited, lowest and highest effective $\chi^{(2)}$ of three different silicon nitride films with different silicon contents. The highest range of tunability is exhibited by the SRN film with a value of $\chi^{(2)}$ as high as 22.7pm/V.

Sample	SiH$_4$ flow rate (sccm)	$\chi^{(2)}_{eff}$ (no bias)(pm/V)	Lowest $\chi^{(2)}_{eff}$ (pm/V)	Highest $\chi^{(2)}_{eff}$ (pm/V)
S$_1$*	180	2.6	2.1	3.9
S$_2$*	276	3.35	2.39	5.93
S$_3$*	500	7.5	3.9	22.7

5.5 Dispersion in the observed nonlinearity

The bulk of the studies on second-order nonlinearities in silicon nitride films have been carried out using either 800nm or 1064nm sources [6, 11]. While the values of nonlinearities reported using these pump wavelengths are relatively high, other works which pursue in-waveguide experiments at a pump wavelength of 1550nm have measured lower values of the nonlinearity [7, 8]. The cause of this discrepancy between values measured using two different pump-wavelengths was attributed previously to a lack of perfect phase-matching in waveguide SHG experiments carried out using a pump at 1550nm.

To test for wavelength dependence in the nonlinearities of our films, we carried out reflection SHG measurements on all three samples, using pumps at 1040nm and 1550nm. These two wavelengths were chosen solely based on source availability. The exact methodology employed in carrying out these measurements is detailed in the supplementary material, while the optical setup is shown in Fig. 3a. To make a fair comparison, parameters such as incident angle, spot size of the beam, average pump power, and polarization state were kept constant while carrying out the measurements across the three samples. Fig. 3b shows the magnitude of the SHG signal, corresponding to the polarization with the maximum second-harmonic signal, generated from the three samples at the two pump-wavelengths. Sample S_3, with the highest silicon content, demonstrates the largest second-harmonic signal among the three samples at both pump wavelengths.

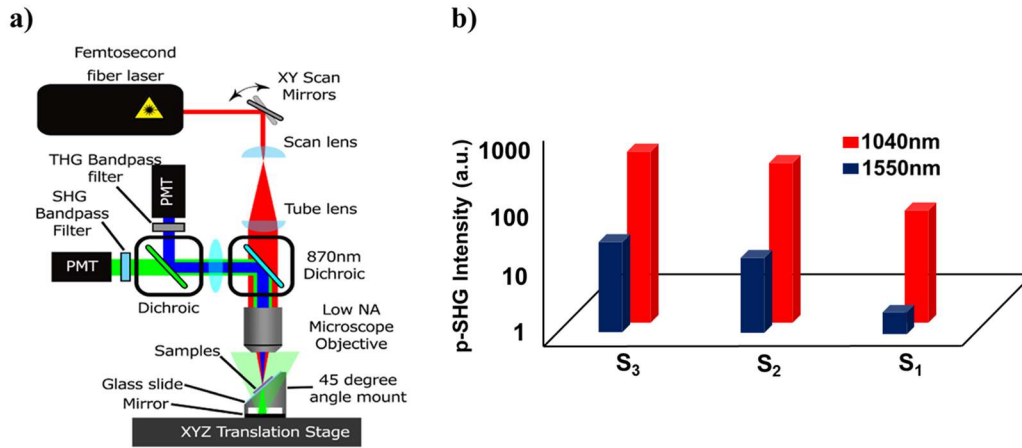Figure. 5.3. (a) Schematic of the reflection mode second-harmonic generation setup. (b) The generated reflected p-polarized SHG signals from the three samples, corresponding to pump wavelengths of 1040 nm (red bars) and 1550 nm (blue bars).

Dispersion in nonlinear susceptibilities is a well-known phenomenon explained by Miller's rule, which defines a relation between dispersion in refractive index and dispersion in second-

51

order nonlinearities [18,19]. Furthermore, work in literature has shown a correlation between increasing silicon content in silicon nitride films and the dispersion in refractive index of such films [20]. These two facts together imply that dispersion in $\chi^{(2)}$ is expected from 1040nm to 1550nm and expected to be the highest in the film with the highest silicon content. However, the magnitude of dispersion demonstrated in this work far exceeds that predicted by Miller's rule and therefore the exact origins of this remains to be explained. Specifically, a difference in magnitude of second harmonic generation between 1040nm and 1550nm of 41, 42 and 39 times is seen across the three films S_3, S_2 and S_1 respectively. Since the power in the second-harmonic signal is proportional to the square of the second-order nonlinear coefficient, this implies that the effective $\chi^{(2)}$ value measured using a 1550nm pump is smaller by up to ~6.4 times than that measured using a 1040nm pump.

5.6 In-waveguide loss characterizations

To characterize the viability of SRN films for on-chip applications, in-waveguide loss measurements were carried out using SRN waveguides on oxide-on-silicon substrates. The thicknesses of the SRN device layer deposited using PECVD, and that of the oxide below were 430nm and 3μm respectively. Ring-resonators coupled to bus waveguides were then fabricated using a combination of electron beam lithography and inductively coupled plasma reactive ion etching (ICP-RIE) using a C_4F_8, SF_6 plasma as outlined in [7]. The waveguide widths were kept at 1000nm, and the coupling gaps were varied from 150-300nm, in the case of TE_0, and from 500-700nm, in the case of TM_0 transmission to achieve critical coupling. The choice of the width and height was made keeping in mind the need to have single-mode operation of both TE- and TM polarized modes at a wavelength of 1550nm. In-waveguide measurements were then performed using a fiber-in, free-space out setup with an Agilent 8164-B tunable CW laser source spanning a

wavelength range of 1.46 to 1.64µm [7,17]. Fig. 4 shows the measured normalized transmission (dB) of the ring-resonators for TE and TM polarizations for the cases closest to the critical coupling regime. This was achieved in the case of TE transmission at a coupling gap of 250nm, and at a gap of 600nm for TM transmission.
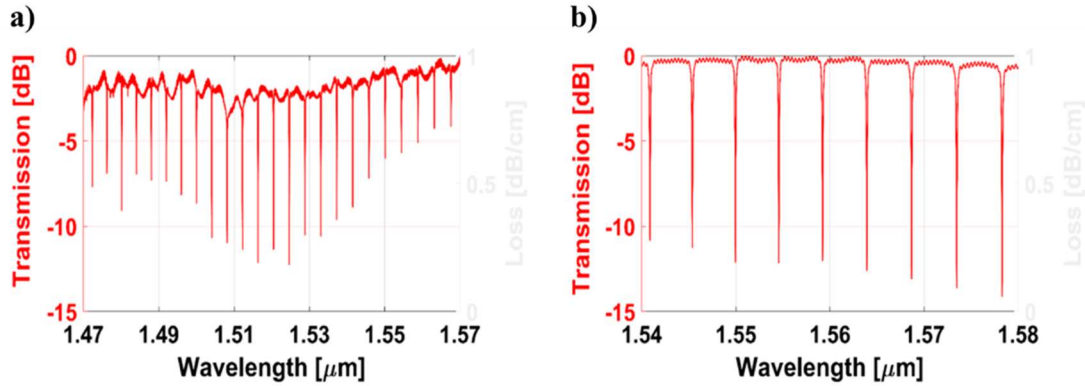
Figure. 5.4. (a)Normalized transmission, across a wavelength range of 1.47 to 1.57µm, of the TE_0 mode in a 1um wide SRN waveguide coupled to a ring-resonator at a coupling gap of 250nm. [17]. (b)Normalized transmission, across a wavelength range of 1.54 to 1.58µm, of the TM_0 mode in a 1um wide SRN waveguide coupled to a ring-resonator at a coupling gap of 600nm.

The propagation loss values for the TE and TM cases, calculated from resonances at 1524.7nm and 1563.9nm, were found to be 9.54 and 14.60 dB/cm respectively [17]. These values, while relatively high when compared to stoichiometric silicon nitride waveguides, are close to other in-waveguide loss measurements for SRN films in literature [14]. Furthermore, these can be improved by optimizing the fabrication process such as the etching recipe and/or employing post-deposition annealing, as well as by increasing the width of the waveguide to reduce sidewall scattering [7]. It should also be noted that the reason for the higher propagation loss observed in the TM case is likely due to the lower confinement of the optical mode in the waveguide core leading to a higher interaction with the top-cladding oxide. Thick PECVD oxides deposited on waveguide structures, are known to have imperfections and air voids leading to higher scattering loss for the propagating modes [7]. Finally, while the results presented here are for the linear losses

in the SRN waveguides, they are expected to exhibit negligible nonlinear losses, such as those due to two photon absorption (TPA). This is discussed extensively in the work by K.J.A. Ooi, et. al. [16], where it is shown that TPA only becomes a dominant loss mechanism in SRN films exceeding a refractive index of 3.

5.7 Conclusions and Discussion

In summary, this work has clearly demonstrated that increasing silicon content in PECVD deposited silicon nitride films results in enhancement in the second-order nonlinearity of such films, achieving a value as high as 8pm/V in as-deposited SRN films. We then demonstrate a relatively large tunability range of the nonlinear coefficient, with a highest demonstrable coefficient of 22pm/V. Furthermore, we demonstrate that the inherent nonlinearity in as-deposited films is highly dispersive, not just in the case of silicon-rich compositions, but also in the case of stoichiometric films. Finally, it is our opinion that the highly dispersive nature of the second-order nonlinearity in these films should be taken into consideration by any future studies.

Chapter 5, in part, contains materials from "On the observation of dispersion in tunable second-order nonlinearities of silicon-rich nitride thin films." published in APL Photonics and co-authored by Hung-Hsi Lin, Alex Friedman, Benjamin M. Cromey, Felipe Vallini, M. W. Puckett, Khanh Kieu, and Yeshaiahu Fainman. The dissertation author was the first author the manuscript.

Chapter 6

Conclusions and Future work

In this thesis, we have demonstrated how different dielectric claddings impact the capacitively-induced electro-optic effect in silicon waveguides. These results are significant because they clearly indicate how the capacitively-induced free-carrier effect may, in waveguides with properly chosen cladding materials, be leveraged to realize CMOS-compatible capacitive electro-optic modulators and wavemixers. Additionally, this thesis demonstrates that a dielectric-clad silicon waveguide's optical losses may be reduced or increased by applying an appropriately chosen bias voltage, allowing for the in-vivo tuning and optimization of a wide variety of photonic devices.

Furthermore, the nonlinear, and, second-order nonlinear properties of silicon nitride thin-films were studied extensively. We have shown for the first time that the bulk second-order nonlinear susceptibilities observed in free-space measurements of silicon nitride thin films may be used in a CMOS-compatible integrated platform to achieve second-harmonic generation which is phase-matched through dispersion engineering of the waveguide geometries. By considering the polarizations of the optical modes relevant to the wavemixing process, we characterized two specific components of the $\chi^{(2)}$ tensor, $\chi^{(2)}_{yyy}$ and $\chi^{(2)}_{xxy}$. We additionally demonstrated how the application of bias voltages across silicon nitride waveguides can lead to an effective increase in their second-order nonlinear susceptibilities and discuss how the enhancement measured here may be improved upon in future work. As new material candidates continue to be considered for the advancement of integrated photonics, we believe characterizations like the ones presented here will be critical in determining which material platform shows the most promise for the realization of a new generation of nonlinear optical devices

Finally, we also demonstrated a large discrepancy of up to an order of magnitude in the nonlinear coefficients of stoichiometric and silicon-rich nitride films. This was done by means of carrying of in-waveguide and free-space measurements, using pumps at 1550nm and 800nm respectively. While this topic was under study, we hypothesized that the discrepancy was due to a lack of perfect phase-matching and/or material changes due to processing during waveguide fabrication. However, upon further analysis, and by carrying out free-space SHG measurements using two different pump-wavelengths, we realized that the second-order nonlinear coefficient was indeed highly dispersive. Considering the results in this thesis, it can be further inferred that this dispersion is ~equally present in both stoichiometric and silicon-rich nitride films. This observed dispersion, it should be noted, is much higher than what can be attributed to Miller's rule, which relates the relative magnitude of the nonlinear susceptibilities to the linear susceptibilities at the respective wavelengths. The exact origin of this high dispersion remains to be explained. Finally, this study's use of thin-films was carefully chosen to be performed in free space to avoid the need for phase matching of any kind, neither all optical quasi-phase matching nor modal dispersion-based phase matching.

The induction and enhancement of second-order nonlinearities is indeed a very promising development for the integrated silicon photonics community. With silicon nitride, increasing becoming a standard material for waveguiding and on-chip applications, this new phenomenon promises to add additional applications and functionalities to the silicon nitride photonics portfolio. It should be noted by any future designers that the increase in nonlinear coefficient does not come at the expense of waveguiding loss. Finally, the results on EFISH, wherein an externally applied electric field can be used to induce an effective second-order nonlinear coefficient, in any material with a third-order nonlinear coefficient, define a clear roadmap towards further improving silicon

nitride's second-order nonlinear properties. This approach, is analogous to the poling of nonlinear

polymers/organics often employed in silicon hybrid devices, but with the added advantage of being

in a low-loss, highly transparent and CMOS compatible material.

Bibliography

Chapter 2

1. R. Jacobsen, K. Anderson, P. Borel, J. Fage-Pederson, L. Frandsen, O. Hansen, M. Kristensen, A. Lavrinenko, G. Moulin, H. Ou, C. Peucheret, B. Zsigri, and A. Bjarklev, "Strained silicon as a new electro-optic material," Nature **441**, 199-202 (2006).

2. B. Chmielak, M. Waldow, C. Matheisen, C. Ripperda, J. Bolten, T. Wahlbrink, M. Nagel, F. Merget, and H. Kurz, "Pockels effect based fully integrated, strained silicon electro-optic modulator," Optics Express **19**, 17212-17219 (2011).

3. B. Chmielak, C. Matheisen, C. Ripperda, J. Bolten, T. Wahlbrink, M. Waldow, H. Kurz, "Investigation of local strain distribution and linear electro-optic effect in strained silicon waveguides," Optics Express **21**, 25324-25332 (2013).

4. P. Damas, X. Le Roux, D. Le Bourdais, E. Cassan, D. Marris-Morini, N. Izard, T. Maroutian, P. Lecoeur, and L. Vivien, "Wavelength dependence of Pockels effect in strained silicon waveguides," Optics Express **22**, 22095-22100 (2014).

5. M. Puckett, J. Smalley, M. Abashin, A. Grieco, and Y. Fainman, "Tensor of the second-order nonlinear susceptibility in asymmetrically strained silicon waveguides: analysis and experimental validation," Opt. Letters **39**, 1693-1696 (2014).

6. X. Zhang, A. Hosseini, H. Subbaraman, S. Wang, Q. Zhan, J. Luo, A. Jen, and R. Chen, "Integrated photonic electromagnetic field sensor based on broadband bowtie antenna coupled silicon organic hybrid modulator." Journal of Lightwave Technology **32**, 3774-3784 (2014).

7. G. Li and P. Yu. "Optical intensity modulators for digital and analog applications." Journal of Lightwave Technology **21**, 9 (2003).

8. C. Schriever, F. Bianco, M. Cazzanelli, M. Ghulinyan, C. Eisenschmidt, J. de Boor, A. Schmid, J. Heitmann, L. Pavesi, and J. Schilling, "Second-Order Optical Nonlinearity in Silicon Waveguides: Inhomogeneous Stress and Interfaces," Advanced Optical Materials **3**, 126-139 (2015).

9. J. Witzens, F. Merget, M. Azadeh, and M. Nezhad, "On the Measurement of the Pockels Effect in Strained Silicon," Optics Letters (accepted).

10. R. Kotipalli, R. Delamare, O. Poncelet, X. Tang, L. Francis, and D. Flandre, "Passivation effects of atomic-layer-deposited aluminum oxide," EPJ Photovoltaics **4**, 45107 (2013).

11. S. Sze and K. Ng, *Physics of Semiconductor Devices,* (Wiley, 1981).

12. S. Dauwe, J. Schmidt, A. Metz, and R. Hezel, "Fixed charged density in silicon nitride films on crystalline silicon surfaces under illumination," Photovoltaic Specialists Conference, 2002, 162-165 (2002).

13. R. Castagne and A. Vapaille, "Apparent interface state density introduced by the spatial fluctuations of surface potential in a M.O.S. structure," Electronics Letters **6**, 691-694 (1970).

14. www.agilent.com

15. T. Tewksbury, H. Lee, and G. Miller, "The Effects of Oxide Traps on the Large-Signal Transient Response of Analogy MOS Circuits," IEEE Journal of Solid-State Circuits **24**, 542-544 (1989).

16.	S. Helland, *Electrical Characterization of Amorphous Silicon Nitride Passivation Layers for Crystalline Silicon Solar Cells*, Ph.D. Thesis, Norwegian University of Science and Technology, Norway (2011).

17.	K. Kwa, S. Chattopadhyay, J. Jankovic, S. Olsen, L. Driscoll, and A. O'Neill, "A model for capacitance reconstruction from measured lossy MOS capacitance–voltage characteristics." Semiconductor science and technology **18**, 82 (2003).

18.	www.silvaco.com

19.	M. Nedeljkovic, R. Soref, G. Mashanovich, "Free-Carrier Electrorefraction and Electroabsorption Modulation Predictions for Silicon Over the 1-14-μm Infrared Wavelength Range," Photonics Journal **3**, 1171-1180 (2011).

20.	www.lumerical.com

Chapter 3

1.	D. Sparacin, S. Spector, and L. Kimerling, "Silicon waveguide sidewall smoothing by wet chemical oxidation." Journal of Lightwave Technology **23**, 2455-2461 (2005).

2.	R. Sharma, M. Puckett, H. Lin, F. Vallini, and Y. Fainman, "Characterizing the effects of free carriers in fully etched, dielectric-clad silicon waveguides." Applied Physics Letters **106**, 241104 (2015).

3.	Lumerical Solutions, Inc. http://www.lumerical.com/tcad-products/fdtd/

4.	Silvaco, Inc. http://www.silvaco.com/

5.	M. Puckett, F. Vallini, A. Grieco, and Y. Fainman, "Multichannel Bragg gratings in silicon waveguides with asymmetric sidewall modulation." Optics Letters **40**, 379-382 (2015).

6.	R. Devine, "Mobile charge, soft breakdown, and self-healing in hydrogen silsesquioxane based intermetal dielectric." Journal of Applied Physics **92**, 3162 (2002).

7.	R. Kotipalli, R. Delamare, O. Poncelet, X. Tang, L. Francis, and D. Flandre, "Passivation effects of atomic-layer-deposited aluminum oxide." EPJ Photovoltaics **4**, 45107 (2013).

8.	T, Takakura, R. Imai, Y. Okamoto, and H. Taniguchi, "Effect of Plasma Pretreatment on Fixed Charge at the Silicon Nitride/Silicon Interface." Japanese Journal of Applied Physics **49**, 046502 (2010).

9.	M. Cazzanelli, F. Bianco, E. Borga, G. Pucker, M. Ghulinyan, E. Degoli, E. Luppi, V. Veniard, S. Ossicni, D. Modotto, S. Wabnitz, R. Pierobon, and L. Pavesi, "Second-harmonic generation in silicon waveguides strained by silicon nitride." Nature Materials **11**, 148-154 (2012).

10.	P. Damas, X. Le Roux, D. Le Bourdais, E. Cassan, D. Marris-Morini, N. Izard, T. Maroutian, P. Lecoeur, and L. Vivien, "Wavelength dependence of Pockels effect in strained silicon waveguides." Optics Express **22**, 22095-22100 (2014).

11.	M. Puckett, J. Smalley, M. Abashin, A. Grieco, and Y. Fainman, "Tensor of the second-order nonlinear susceptibility in asymmetrically strained silicon waveguides: analysis and experimental validation." Optics Letters **39**, 1693-1696 (2014).

12.   R. Jacobsen, K. Andersen, P. Borel, J. Fage-Pedersen, L. Frandsen, O. Hansen, M. Kristensen, A. Lavrinenko, G. Moulin, H. Ou, C. Peucheret. B. Zsigri, and A. Bjarklev, "Strained silicon as a new electro-optic material." Nature **441**, 199-202 (2006).

13.   B. Chmielak, M. Waldow, C. Matheisen, C. Ripperda, J. Bolten, T. Wahlbrink, M. Nagel, F. Merget, and H. Kurz, "Pockels effect based fully integrated, strained silicon electro-optic modulator." Optics Express **19**, 17212-17219 (2011).

14.   B. Chmielak, C. Matheisen, C. Ripperda, J. Bolten, T. Wahlbrink, M. Waldow, and H. Kurz, "Investigation of local strain distribution and linear electro-optic effect in strained silicon waveguides." Optics Express **21**, 25324-25332 (2013).

15.   M. Nedeljkovic, R. Soref, and G. Mashanovich, "Free-Carrier Electrorefraction and Electroabsorption Modulation Predictions for Silicon Over the 1–14um Infrared Wavelength Range." Photonics Journal, IEEE **3**, 1171-1180 (2011).

16.   L. Alloatti, M. Lauermann, C. Surgers, C. Koos, W. Freude, and J. Leuthold, "Optical absorption in silicon layers in the presence of charge inversion/accumulation or ion implantation." Applied Physics Letters **103**, 051104 (2013).

17.   L. Pavesi and D. Lockwood, Silicon Photonics, Springer (2004).

18.   W. Bogaerts, P. De Heyn, T. Van Vaerenbergh, K. De Vos, S. Selvaraja, T. Claes, P. Dumon, P. Bienstman, D. Van Thourhout, and R. Baets, "Silicon microring resonators." Laser and Photonics Reviews **6**, 47-73 (2012).

19.   J. Niehusmann, A. Vörckel, P. H. Bolivar, T. Wahlbrink, W. Henschel, and H. Kurz, "Ultrahigh-quality-factor silicon-on-insulator microring resonator." Optics letters **29**, 2861-2863 (2004).

20.   C. Xiong, W. Pernice, and H. Tang, "Low-loss, silicon integrated, aluminum nitride photonic circuits and their use for electro-optic signal processing." Nanoletters **12**, 3562-2568 (2012).

21.   S. Grillanda, and F. Morichetti, "Light-induced metal-like surface of silicon photonic waveguides." Nature communications **6** (2015).

22.   S. Keyvaninia, M. Karvar, and A. Bahrampour, "Dynamic behavior of electric field in the microrings in the presence of Kerr and two-photon absorption." Proceedings of SPIE **6996**, Silicon Photonics and Photonic Integrated Circuits, 69961X (2008).

23.   M. Bazilchuk, H. Haug, and E. Marstein, "Modulating the fixed charge density in silicon nitride films while monitoring the surface recombination velocity by photoluminescence imaging." Applied Physics Letters **106**, 143505 (2015).

Chapter 4

1.   B. Jalali and S. Fathpour, "Silicon photonics," Journal of Lightwave Technology **24**, 4600-4615 (2006).

2.   R. Soref, "Mid-infrared photonics in silicon and germanium," Nature Photonics **4**, 495-497 (2010).

3. M. Dinu, F. Quochi, and H. Garcia, "Third-order nonlinearities in silicon at telecom wavelengths," Applied Physics Letters **82**, 2954 (2003).

4. A. Bristow, N. Rotenberg, and H. van Driel, "Two-photon absorption and Kerr coefficients of silicon for 850-2200 nm," Applied Physics Letters **90**, 191104 (2007).

5. Michal Lipson, "Compact electro-optic modulators on a silicon chip," IEEE Journal of Selected Topics in Quantum Electronics **12,** 1520 (2006).

6. R. Jacobsen, K. Andersen, P. Borel, J. Fage-Pedersen, L. Frandsen, O. Hansen, M. Kristensen, A. Lavrinenko, G. Moulin, H. Ou, C. Peucheret, B. Zsigri, and A. Bjarklv, "Strained silicon as a new electro-optic material," Nature **441**, 199-202 (2006).

7. M. Cazzanelli, F. Bianco, E. Borga, G. Pucker, M. Ghulinyan, E. Degoli, E. Luppi, V. Veniard, S. Ossicini, D. Modotto, S. Wabnitz, R. Pierobon, and L. Pavesi, "Second-harmonic generation in silicon waveguides strained by silicon nitride," Nature Materials **11**, 148-154 (2012).

8. B. Chmielak, M. Waldow, C. Matheisen, C. Ripperda, J. Bolten, T. Wahlbrink, M. Nagel, F. Merget, and H. Kurz, "Pockels effect based fully integrated, strained silicon electro-optic modulator," Optics Express **19**, 17212-17219 (2011).

9. M. Puckett, J. Smalley, M. Abashin, A. Grieco, and Y. Fainman, "Tensor of the second-order nonlinear susceptibility in asymmetrically strained silicon waveguides: analysis and experimental validation," Optics Letters **39**, 1693-1696 (2014).

10. K. Ikeda, R. Saperstein, N. Alic, and Y. Fainman, "Thermal and Kerr nonlinear properties of plasma-deposited silicon nitride/silicon dioxide waveguides," Optics Express **17**, 12987-12994 (2008).

11. C. Torres-Torres, A. Lopez-Suarez, L. Tamayo-Rivera, R. Rangel-Rojo, A. Crespo-Sosa, J. Alonso, and A. Oliver, "Thermo-optic effect and optical third order nonlinearity in nc-Si embedded in a silicon-nitride film," Optics Express **16**, 18390-18396 (2008).

12. D. Moss, R. Morandotti, A. Gaeta, and M. Lipson, "New CMOS-compatible platforms based on silicon nitride and Hydex for nonlinear optics," Nature Photonics **7**, 597-607 (2013).

13. J. Levy, A. Gondarenko, M. Foster, A. Turner-Foster, A. Gaeta, and M. Lipson, "CMOS-compatible multiple-wavelength oscillator for on-chip optical interconnects," Nature Photonics **4**, 37-40 (2010).

14. S. Khan, J. Chile, J. Ma, and S. Fathpour, "Silicon-on-nitride waveguides for mid-and near-infrared integrated photonics," Applied Physics Letters **102**, 121104 (2013).

15. T. Ning, H. Pietarinen, and O. Hyvarinen, "Strong second-harmonic generation in silicon nitride films," Applied Physics Letters **100**, 161902 (2012).

16. J. Levy, M. Foster, A. Gaeta, and M. Lipson, "Harmonic generation in silicon nitride ring resonators," Optics Express **19**, 11415-11421 (2011).

17. W. N. Herman, and L. M. Hayden, "Maker fringes revisited: second-harmonic generation from birefringent or absorbing materials," JOSA B **12**, 416-427 (1995).

18. T. Suhara, M. Fujimura, *Waveguide Nonlinear Optic Devices*, Springer (2003).

19.   COMSOL, Inc., http://www.comsol.com

20.   M. Puckett, F. Vallini, A. Grieco, and Y. Fainman, "Multichannel Bragg gratings in silicon waveguides with asymmetric sidewall modulation," Optics Letters **40**, 379-382 (2015).

21.   R. Sharma, M. Puckett, H. H. Lin, A. Isichenko, F. Vallini, and Y. Fainman, "Effect of dielectric claddings on the electro-optic behavior of silicon waveguides," Optics letters, **41**, 1185-1188 (2016).

22.   X. Guo, C. Zou, C. Schuck, H. Jung, R. Cheng, and H. Tang, "Parametric down-conversion photon pair source on a nanophotonic chip," arXiv:1603.0372v1 (2003).

23.   Y. Wang, Y. Wang, L. Cao, and Z. Cao, "High-efficiency visible photoluminescence from amorphous silicon nanoparticles embedded in silicon nitride," Applied Physics Letters **83**, 3474-3476 (2003).

24.   M. Bortz, S. Field, M. Fejer, D. Nam, R. Waarts, and D. Welch, "Noncritical quasi-phase-matched second harmonic generation in an annealed proton-exchanged LiNbO3 waveguide," IEEE Journal of Quantum Electronics **30**, 2953-2960 (2002).

25.   H. Wagner, M. Kuhnelt, W. Langbein, and J. Hvam, "Dispersion of the second-order nonlinear susceptibility in ZnTe, ZnSe, and ZnS," Physics Review B **58**, 10494 (1998).

26.   J. Khurgin, T. Stievater, M. Pruessner, and W. Rabinovich, "On the origin of the second-order nonlinearity in strained Si–SiN structures," Journal of the Optical Society of America B **32**, 2494-2499 (2015).

27.   T. Ning, C. Tan, T. Niemi, M. Kauranen, and G. Genty, "Enhancement of second-harmonic generation from silicon nitride with gold gratings," Optics Express **23**, 30695-30700 (2015).

28.   N. Bloembergen, *Nonlinear Optics*, World Scientific (1996).

29.   S. Minisalle, S. Yerci, and L. Dal Negro, "Nonlinear optical properties of low temperature annealed silicon-rich oxide and silicon-rich nitride materials for silicon photonics," Applied Physics Letters **100**, 021109 (2012).

Chapter 5

1.   C. Malgrange, C. Ricolleau, and M. Schlenker, "Symmetry and Physical Properties of Crystals," (Springer, 2014).

2.   R. S. Jacobsen, Karin N. Andersen, Peter I. Borel, Jacob Fage-Pedersen, Lars H. Frandsen, Ole Hansen, Martin Kristensen Lavrinenko, A.V., Moulin, G., Ou, H. and Peucheret, C., Nature **441**, no. 7090 (2006): 199.

3.   M. Cazzanelli, F. Bianco, E. Borga, G. Pucker, M. Ghulinyan, Elena Degoli, E. Luppi, V. Véniard, S. Ossicini, D. Modotto, and S. Wabnitz, Nature materials **11**, no. 2 (2012): 148.

4.   D. J. Moss, R. Morandotti, A. L. Gaeta, and Michal Lipson, Nature photonics **7**, no. 8 (2013): 597.

5.   J. S. Levy, M. A. Foster, A. L. Gaeta, and M. Lipson, Optics express **19**, no. 12 (2011): 11415-11421.

6.   T. Ning, H. Pietarinen, O. Hyvarinen, J. Simonen, G. Genty, and M. Kauranen, Appl. Phys. Lett. **100**, 161902 (2012). ⌞SEP⌟

7.   M. W. Puckett, R. Sharma, H. Lin, M. Yang, F. Vallini, and Y. Fainman, Opt. Express **24**, 16923 (2016). ⌞SEP⌟

8.   Billat, D. Grassani, M. HP Pfeiffer, S. Kharitonov, T. J. Kippenberg, and Camille-Sophie Brès, Nature communications **8**, no. 1 (2017): 1016.

9.   Kitao, K. Imakita, I. Kawamura and M. Fujii, J. Phys. D: Appl. Phys **47**, 215101 (2014).

10.   H. Lin, R. Sharma, M. Yang, , M . W. Puckett, C. D. Wurm, F. Vallini, and Y. Fainman, 2017, May. In CLEO: Science and Innovations (pp. SM1M-6). Optical Society of America.

11.   K. Koskinen, R. Czaplicki, A. Slablab, T. Ning, Artur Hermans, Bart Kuyken, V. Mittal, G. S. Murugan, T. Niemi, R. Baets, and Kauranen, M. Optics letters **42**, no. 23 (2017): 5030-5033.

12.   H. Lin, M. Yang, R. Sharma, M. W. Puckett, S. Montoya, C. D. Wurm, F. Vallini, E. E. Fullerton, and Y. Fainman, Appl. Phys. Lett. **110**,113103 (2017).

13.   H. Lin, F. Vallini, M. Yang, R. Sharma, M. W. Puckett, S. Montoya, C. D. Wurm, E. E. Fullerton & Y. Fainman, Scientific Reports **7**, 9983 (2017).

14.   J. W. Choi, G. F. R. Chen, D. K. T. Ng, K. J. A. Ooi, and D. T. H. Tan, Scientific reports **6** (2016): 27120.

15.   Lacava, S. Stankovic, A. Z. Khokhar, T. D. Bucio, F. Y. Gardes, G. T. Reed, David J. Richardson, and Periklis Petropoulos, Scientific reports **7**, no. 1 (2017): 22.

16.   K. J. A. Ooi, D. K. T. Ng, T. Wang, A. K. L. Chee, S. K. Ng, Q. Wang, L. K. Ang, A. M. Agarwal, L. C. Kimerling, and D. T. H. Tan, Nature communications **8** (2017): 13878.

17.   R. Sharma, M. W. Puckett, H. Lin, A. Isichenko, F. Vallini, and Y. Fainman, Opt. Lett. **41**, 6 (2016).

18.   R. C. Miller, Applied Physics Letters **5.1** (1964): 17-19.

19.   Hermans, C. Kieninger, K. Koskinen, A. Wickberg, E. Solano, J. Dendooven, M. Kauranen, S. Clemmen, M. Wegener, C. Koos, and R. Baets, Scientific reports **7** (2017): 44581

20.   K. Koskinen, R. Czaplicki, A. Slablab, T. Ning, A. Hermans, B. Kuyken, V. Mittal, G. S. Murugan, T. Niemi, R. Baets, and M. Kauranen, *Optics letters* **42**, no. 23 (2017): 5030-5033.

21.   M. A. G. Porcel, , J. Mak, C. Taballione, V. K. Schermerhorn, J. P. Epping, P. J. M. V. D. Slot, and K. J. Boller, *Optics express* **25**, no. 26 (2017): 33143-33159.